2016

Investigating the Structure of the Papain-Inhibitor Complex using SPR and NMR

Margaret Sara Thomasson
Louisiana State University and Agricultural and Mechanical College

INVESTIGATING THE STRUCTURE OF THE PAPAIN-INHIBITOR
COMPLEX USING SPR AND NMR

A Dissertation

Submitted to the Graduate Faculty of the
Louisiana State University and
Agricultural and Mechanical College
in partial fulfilment of the
requirements for the degree of
Doctor of Philosophy

in

The Department of Chemistry

by
Margaret Sara Thomasson
B.S., College of Charleston, 2010
August 2016

For Mom and Dad, who challenge, love, and encourage me.

For Curry, who picks me up the most.

For everyone who reminded me that I could – Guess what? I did.

"Think for yourself, and question." – Lorin Ashton

ACKNOWLEDGMENTS

It takes a village to raise a child, so I suppose it makes sense that it would take an incredible network of people to help a 20-something survive graduate school.

Allow me to begin by thanking Dr. Megan Macnaughtan, my advisor. Without her support, guidance, and extreme patience, I would not still be here. Joining her research group pulled me out of my comfort zone and away from the kind of chemistry I knew. It was difficult (and I know I whined about it at least a few times) but in the end, I'm glad it happened. To my labmates, Abigael, Amid, Huimin, and Thilini: it has been a pleasure to share lab space with you all. I know you will all find success wherever the future takes you. Dr. Octavia Goodwin, you are a brilliant scientist, and a great friend. Stay awesome.

To Tsu, my Someone, who was willing to call me at 2am and tell me to wake up and get back to work: you've stuck with me ever since, helping me carry on through all of the blood, sweat, and tears that have gone into this research these past few years. Thanks, partner. I love you.

Is it silly to thank the internet? I feel I should. Thank you, internet. You allowed me to contact my precious people from all corners of the world, which is the best source of sanity. Thank you especially to Curry, Saffron, Brenna, Brona, Tony, Lela D, Emily, Jchan, Alicia, Lacy, Lysa, Kelsey, Paulina, Ryin… Some were here from the beginning, others joined along the way, but all of you have helped me through this. It's impossible to name everyone who matters. I wish I could.

I doubt my parents knew for certain they had a scientist to raise, they were likely too focused on the nearly impossible task of keeping her alive and well – no matter how many trees she fell from, how many crosswalks she ignored, how hard she fought against doing what she was told, or how many tears she cried on their shoulders. This is for them, their love and support.

Thank you, everyone. I love you all.

TABLE OF CONTENTS

ABSTRACT

Cysteine proteases (CPs) are enzymes with a nucleophilic thiol in their active sites. Inhibitors of cysteine proteases (ICPs) occur naturally in bacterial pathogens and some protozoa. In parasites, ICPs are often virulence factors, contributing to the formation and survival of amastigotes within host cells. These amastigotes have higher CP activity, therefore making both ICPs and CPs potential drug targets. Despite great genetic variability, ICPs contain highly conserved structural features, including a series of defined loops that play a significant role in binding CPs. Papain, a CP from *Carica papaya*, complexes with ICP from *Leishmania mexicana*. Although the individual 3-D structures of ICP and papain have been determined, as of this work, the structure of the papain-ICP complex has only been predicted, not solved.

This research details the development of a technique for determining quaternary structure of the papain-ICP complex using paramagnetic relaxation enhancement NMR (PRE-NMR). A paramagnetic tag (MTSL) was added to various cysteine-mutants of ICP to measure distances to reductively ^{13}C-methylated papain. The modification of ICP with MTSL was quantified using EPR, and the effects of labeling on the binding kinetics of papain and ICP were determined using SPR. ^{13}C-methyl peak perturbations due to PRE were observed when papain was bound to spin-labeled E102C-ICP and K27C-ICP. Intermolecular distances were predicted using modeling software and a working model of the complex was created. Data from additional mutants will help to further determine complex structure and perfect the model.

The penultimate chapter of this dissertation includes work towards the development of a method for studying protein-protein interactions using atomic force microscopy. Papain-ICP was used as a model system, with the intention to apply this method to the study of another system: filamentous actin (f-actin) and the actin-binding domain of abelson tyrosine-protein kinase

(ABL2-FABD). The creation of nanopores on an AFM sensor chip surface was successful. ICP monomers bound selectively into the pores. Attempts to form the papain-ICP complex on the chip surface were unsuccessful, and future work is needed to perfect this method. The final chapter of this dissertation is a literature review outlining previous work in this area.

CHAPTER 1: BACKGROUND

1.1. The Importance of Protein Structure in Protein Function

Protein structure is categorized by four tiers: primary, secondary, tertiary, and quaternary (1). Primary structure, the amino acid sequence of a protein, gives information on the chemical properties of the protein at any position along the protein chain. Each amino acid residue has a different chemical structure, therefore different types of chemistry occur at different positions along the protein chain. Secondary structure refers to the formation of beta sheets or alpha helixes along the protein chain, or to unstructured regions referred to as loops. Tertiary structure refers to the interaction of secondary structural elements, causing the protein to fold. This is the shape the protein takes in its natural, functional state. The final tier of protein structure, quaternary structure, describes the way that two proteins bind to form a complex.

Protein function is dependent on the structure of the protein (1). In order for proteins to carry out their functions, they often must be folded in a specific conformation that directly aids activity. For example, enzyme activity is dependent on the position of amino acids in the active site and their availability to bind to other proteins or small molecules. If the active site is hindered, blocked, or altered due to improper folding, binding will not occur. The more that is known about the structure of a protein, the more our understanding about its function in biological processes increases.

1.2. Protein-Protein Interactions

Over 80% of proteins function through complex formation in biological systems (1). Protein-protein interactions dictate the function and activity of individual proteins, as well as their use in overall processes. This significant impact makes the study of these interactions imperative for biochemical and biomedical research. Potential drug targets can be identified

through the study of protein-protein interactions, which can lead to the development of disease treatments, therapies, regulations, or vaccines (2).

1.3. Cysteine Proteases and Their Inhibitors

Cysteine proteases (CPs) are enzymes that degrade proteins by reacting with basic side chains of adjacent amino acids, typically histidine (3). They have a molecular mass in the range of 21-30 kDa. The family of CPs that has been the most extensively characterized is the papain family, (3) which is comprised of CPs that are structurally related to papain, a CP naturally present in the papaya fruit (*Carica papaya*). Papain is a 23.4 kDa protein with 212 residues. It is extracted from the latex of the unripe fruit and is used in many health and beauty products, such as teeth whitening and skin care. All CPs in the papain family contain a two-domain structure with an active site between them containing the catalytic residues of cysteine-25 and histidine-159 (4).
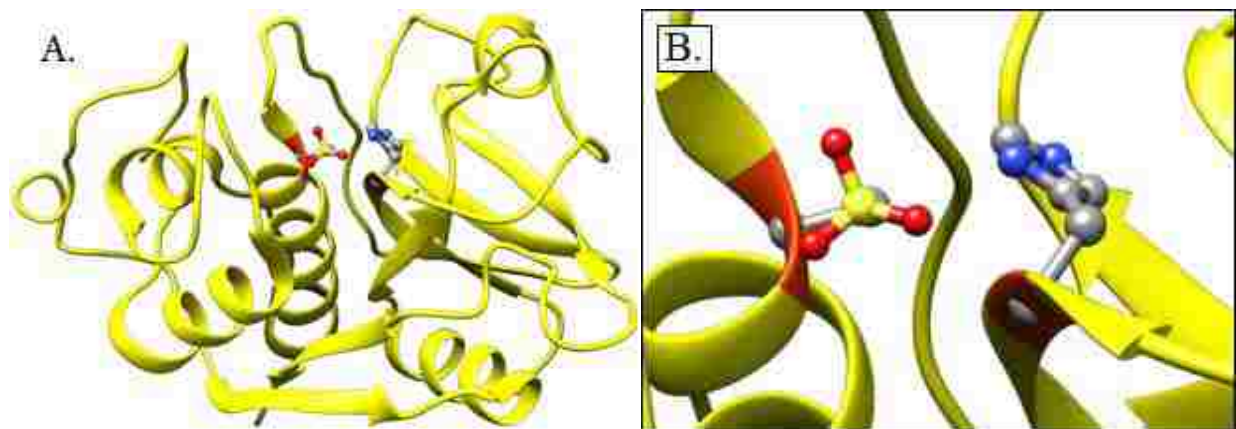
Figure 1.1: (A) The structure of papain from *Carica papaya*, from the Protein Data Bank, ID#: 9PAP. (B) Zoom: atoms shown are the catalytic residues C25 and H159, located on either side of the catalytic cleft. Standard color convention is used: red for hydrogen, yellow for sulfur, blue for nitrogen, gray for carbon.

Protease inhibitors are molecules that inhibit protease functions. Many of these are proteins that naturally occur. In 2004, Rawlings et al. proposed a classification system to better streamline the availability of and access to information about protease inhibitors (5). This system

is organized first by assigning the inhibitors to 85 families (as of 2015) based on similarities in amino acid sequence. Further classification involves the grouping of families into clans when there is evidence that members of two families are distantly related to each other through tertiary structure. This classification system is available as a database that can be accessed electronically. (6)

Cysteine protease inhibitors are proteins that specifically inhibit the activity of CPs. Multiple clans and families of protease inhibitors exhibit activity for papain-like CPs, such as the cystatin super-family (clan IH, family I25) (7) and clan IX, family I31 (8). Recently, the chagasin family (clan I-, family I42) has been found to also inhibit papain-like CPs in both parasites and mammals (9). Members of family I42 are specifically called ICPs. According to the MEROPS database, family I42 contains 168 protein sequences. Of these proteins, four were given MEROPS identifiers, signifying that enough is known about the protein to merit being given an identifier. This could be information such as one or more amino acid sequence, or information about substrate specificity (7). Two of these proteins also have PDB entries: chagasin and amoebiasin-2. It has also been found that inhibition is reversible and tight-binding (9). Family I42 family members appear in some parasitic protozoa (such as *Trypanosoma cruzi*), and some bacteria (such as *Pseudomonus aeruginosa*). Nevertheless, these proteins do not appear to be similar in amino acid sequence, but there is evidence that some highly conserved structural motifs between ICPs are what contribute to their activity (10).

1.4. *L. mexicana* ICP – Structural Conservations in Lieu of Sequence Consistency

Though ICPs from protozoa and bacteria share only a low percentage of sequence homology, they are all effective inhibitors of papain-like CPs due to similar tertiary structures at the point of interaction. According to Sanderson et al., there are three highly conserved sequence

motifs: LXS/GNPTTGY/FXW, L/MV/LGA/XGG, and LV/XYXRPW/F (11). These motifs may

be involved in binding papain-like CPs, pointing to the formation of similar tertiary structure. It

has also been determined that the addition of a 6x-His-tag to the N-terminus of ICPs does not

affect inhibition. This information suggests that, unlike the cystatin family of cysteine protease

inhibitors (family I25) (12), the N-terminal region is not involved in ICP-CP interaction for

family I42 ICPs .
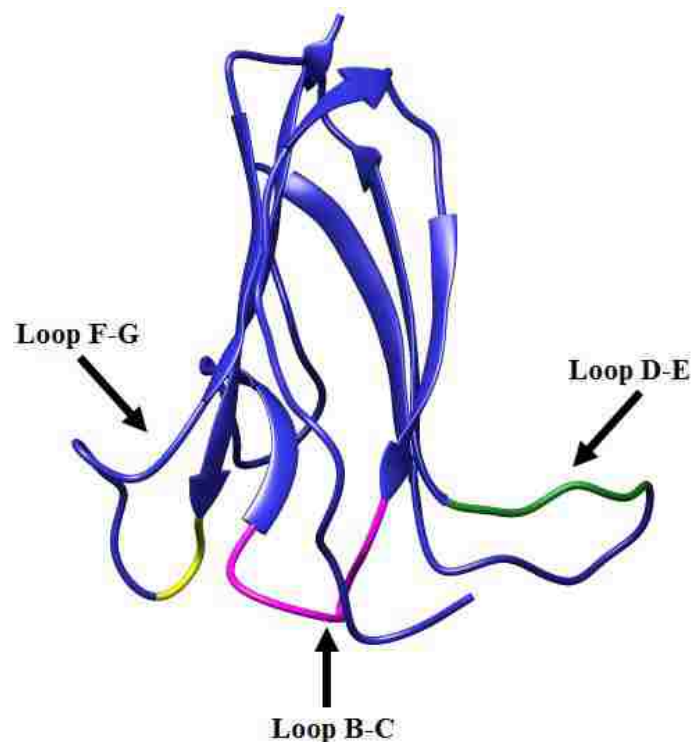
Figure 1.2: The structure of ICP from *L. mexicana*, from the Protein Data Bank. (ID#: 2C34) Highlighted are the three conserved structural motifs: loop B-C, GNPTTGY (magenta); loop D-E, MVGVGG (green); and loop F-G, RPF (yellow).

A clan I-, family I42 ICP from the parasite *Leishmania mexicana* was used in this study.

This ICP appears to regulate enzyme activity in the host that the parasite infects, making it a

strong virulence factor for the parasite. Over-expression of ICP in the parasite shows a

significant decrease in virulence *in vivo*. Interestingly, the infectivity of ICP null mutants in mice

was reduced as well (13). Consistent with the observation that ICPs have low sequence

homology, *L. mexicana* ICP has only 31% identity with ICP from *T. cruzi,* and 25% identity with ICP of *P. aeruginos* (11). Its structure was determined by NMR by Brian Smith and coworkers in 2006 (10). They confirmed residues key for inhibitory activity and created a preliminary model of its possible interaction with both papain and a *L. mexicana* CP known as CPB (14). In solution, ICP adopts an immunoglobulin-like fold. It contains seven beta-strands, with one sheet formed by anti-parallel strands B, E, and D. The other is formed by parallel strands G, F, and C, along with strand A in parallel to strand G. These beta-sheets surround a hydrophobic core of other residues. The three highly conserved motifs appear once again here, with all three located in the loops at one end of the molecule, which suggests the CP-binding site. Furthermore, residues in the D-E loop are critical for CP-binding, as proteins with mutations in the D-E loop lacked activity toward the native CP in *L. mexicana.*

1.5. The Papain-ICP Complex

Although *L. mexicana* ICP does not encounter papain naturally, given their separate natural environments, ICP and papain bind in a tight-binding 1:1 ratio. The papain-ICP complex has been previously modeled by Brian Smith, et al, and is shown in Figure 1.3 (10). The model was constructed using information derived from chemical shifts in NMR spectra when ICP is bound to papain, and was supplemented with information from the crystal structure of papain in complex with stefin B (Protein Data Bank ID#: 2CIO), another cysteine protease inhibitor in the same family. Very few amino acids of ICP are resolved in the x-ray structure, and more information that is specific to the interaction between papain and ICP is needed. Additionally, computational data sets disagree on whether loop B-C or D-E of ICP is the more important loop in inhibiting papain or other CPs (10). When the work detailed in this dissertation began, ICP was unique. Although a homologous structure has been found since the project began, (15) as of

this work, the structure of the papain-ICP complex has not yet been fully solved. Because CPs are ideal drug targets for many neglected diseases (for example, leishmaniasis, which is caused by the bite of the *L. mexicana* sand fly), it is important to fully understand the interaction of ICPs and their CPs.
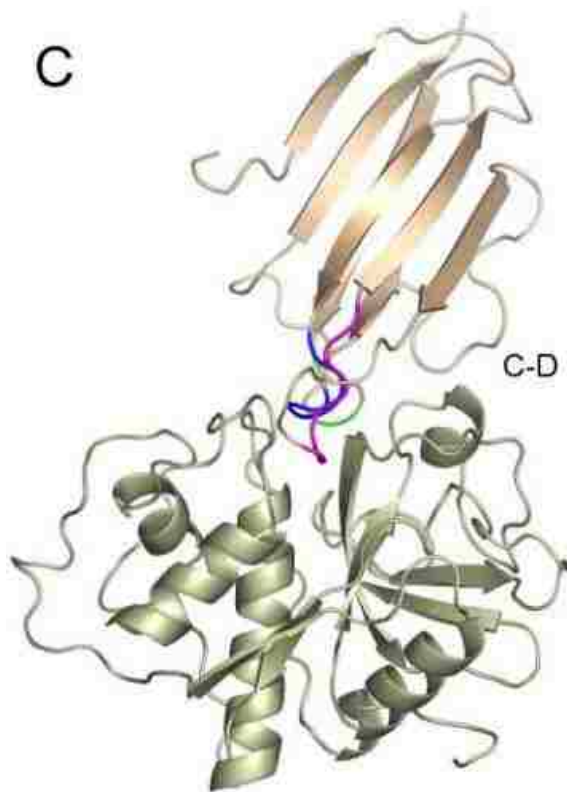
Figure 1.3: A model of the complex of *L. mexicana* ICP and papain. Adapted from Smith, et al. and used with permission (10).

1.6. Conclusion

The work in this dissertation has two goals. The first goal is to develop a method to determine the interaction surface on a cysteine protease inhibitor for binding the cysteine protease papain. Surface plasmon resonance (SPR) was used for method development and analysis. The second goal of this dissertation is to determine the structure of the papain-inhibitor complex using paramagnetic relaxation enhancement NMR (PRE-NMR), which will give us the data we need to determine the quaternary structure of the complex.

The penultimate chapter of this dissertation involves the development of an AFM technique to observe protein-protein interactions. The papain-ICP complex was used as a model for method development with the intention of applying this technique to studying the complex formed between the actin binding domain of abelson tyrosine-protein kinase (ABL2-FABD) and filamentous actin (F-actin). Finally, the dissertation concludes with a review of microscopy basics for the study of actin with actin-binding proteins, which was previously published in *Analytical Biochemistry* volume 443, issue 2 (16).

1.7. References

1.   Nelson, D. L., Cox, M. M., and Lehninger, A. L. (2013) *Lehninger principles of biochemistry*, W.H. Freeman, New York

2.   Szasz, J., Yaffe, M. B., and Sternlicht, H. (1993) Site-directed mutagenesis of alpha-tubulin. Reductive methylation studies of the Lys 394 region. *Biophys J* **64**, 792-802

3.   Mitchel, R. E., Chaiken, I. M., and Smith, E. L. (1970) The complete amino acid sequence of papain. Additions and corrections. *J. Biol. Chem.* **245**, 3485-3492

4.   Grzonka, Z. J., Elżbieta, Kasprzykowski, F., Kasprzykowska, R., Łankiewicz, L., Wiczk, W., Wieczerzak, E., Ciarkowski, J., Drabik, P., Janowski, R., Kozak, M., Jaskólski, M., and Grubb, A. (2001) Structural studies of cysteine proteases and their inhibitors. *Acta Biochim. Pol.* **48**, 1-20

5.   Rawlings, N. D., Tolle, D. P., and Barrett, A. J. (2004) Evolutionary families of peptidase inhibitors. *Biochem. J.* **378**, 705-716

6.   Rawlings, N. D., Waller, M., Barrett, A. J., and Bateman, A. (2014) MEROPS: The database of proteolytic enzymes, their substrates and inhibitors. *Nucleic Acids Res.* **42**, D503-509

7.   Rawlings, N. D., Tolle, D. P., and Barrett, A. J. (2004) MEROPS: The peptidase database. *Nucleic Acids Res.* **32**, D160-164

8.   Guncar, G., Pungercic, G., Klemencic, I., Turk, V., and Turk, D. (1999) Crystal structure of MHC class II-associated p41 Ii fragment bound to cathepsin L reveals the structural basis for differentiation between cathepsins L and S. *EMBO J.* **18**, 793-803

9.   Monteiro, A. C., Abrahamson, M., Lima, A. P., Vannier-Santos, M. A., and Scharfstein, J. (2001) Identification, characterization and localization of chagasin, a tight-binding cysteine protease inhibitor in *Trypanosoma cruzi*. *J. Cell. Sci.* **114**, 3933-3942

10. Smith, B. O., Picken, N. C., Westrop, G. D., Bromek, K., Mottram, J. C., and Coombs, G. H. (2006) The structure of *Leishmania mexicana* ICP provides evidence for convergent evolution of cysteine peptidase inhibitors. *J. Biol. Chem.* **281**, 5821-5828

11. Sanderson, S. J., Westrop, G. D., Scharfstein, J., Mottram, J. C., and Coombs, G. H. (2003) Functional conservation of a natural cysteine peptidase inhibitor in protozoan and bacterial pathogens. *FEBS Lett.* **542**, 12-16

12. Mason, R. W., Sol-Church, K., and Abrahamson, M. (1998) Amino acid substitutions in the N-terminal segment of cystatin C create selective protein inhibitors of lysosomal cysteine proteinases. *Biochem. J.* **330**, 833-838

13. Besteiro, S., Coombs, G. H., and Mottram, J. C. (2004) A potential role for ICP, a leishmanial inhibitor of cysteine peptidases, in the interaction between host and parasite. *Mol. Microbiol.* **54**, 1224-1236

14. Sanderson, S. J., Pollock, K. G., Hilley, J. D., Meldal, M., Hilaire, P. S., Juliano, M. A., Juliano, L., Mottram, J. C., and Coombs, G. H. (2000) Expression and characterization of a recombinant cysteine proteinase of *Leishmania mexicana. Biochem. J.* **347**, 383-388

15. Redzynia, I., Ljunggren, A., Bujacz, A., Abrahamson, M., Jaskolski, M., Bujacz, G. (2009) Crystal structure of the parasite inhibitor chagasin in complex with papain allows identification of structural requirements for broad reactivity and specificty determinants for target proteases. *FEBS J.* **276**, 93-806

16. Thomasson, M. S., and Macnaughtan, M. A. (2013) Microscopy basics and the study of actin–actin-binding protein interactions. *Anal. Biochem.* **443**, 156-165

CHAPTER 2: INVESTIGATING THE EFFECTS OF STERIC HINDRANCE ON PAPAIN-ICP BINDING USING SURFACE PLASMON RESONANCE

2.1. Introduction

Papain is a cysteine protease (CP), which is an enzyme with a nucleophilic thiol (cysteine residue) in its active site to cleave peptide bonds (1). CPs are often virulence factors, which makes them potential drug targets (2). Inhibitors of cysteine proteases (ICPs) contain highly conserved structural features, suggesting important regions for ICP-CP interactions (3). Most of these sites are conventionally predictable, but complex structure, steric hindrance, or properties of the binding site can all affect ICP-CP interactions. Additionally, modifications that are necessary to study the papain-ICP complex with NMR, such as reductive methylation of papain, may interfere with complex formation. It is important to confirm that the complex still forms even when papain has been reductively methylated.

Here, we investigate the effects of steric hindrance on papain-ICP binding using surface plasmon resonance (SPR) when the ICP is anchored to a surface in various orientations. Results using unmodified papain were compared to results using reductively methylated papain (RM-papain) to ensure that the added methyl groups do not interfere with the formation of the papain-ICP complex.

2.2. Materials

Two pET28 plasmids encoding *Leishmania mexicana* ICP with an N-terminal 6XHis-tag were supplied by Brian O. Smith, University of Glasgow. Papain from papaya latex (*Carica papaya*), isopropyl β-D-1-thiogalactopyranoside (IPTG), kanamycin, sodium dodecyl sulfate (SDS), sodium chloride (NaCl), sodium phosphate monobasic, potassium phosphate monobasic, imidazole, nickel chloride, ethylenediaminetetraacetic acid (EDTA), HEPES, tween, ammonium sulfate, dimethylamine borane (DMAB), tris(hydroxymethyl)aminomethane (tris), formaldehyde,

glycine, ethanol, and methanol were purchased from Sigma-Aldrich. Tris(2-carboxyethyl)phosphine hydrochloride (TCEP), Coomassie Plus Protein assay, and bovine serum albumin protein standard were purchased from Pierce. All SDS-polyacrylamide gel electrophoresis (SDS-PAGE) materials (gels, tank, lid, power source, sample buffer) and Sephadex G50-medium were purchased from Bio-Rad. Ni Sepharose FastFlow media and a Sephacryl S-100 chromatography column were purchased from GE Healthcare. Poly-NTA derivatized linear polycarboxylate hydrogel SPR chips were purchased from Xantec. All water used was supplied from a Millipore Direct-Q 3 ultrapure water system.

2.3. Expression and Purification of *L. mexicana* ICP Mutants

Two pET28 plasmids encoding *L. mexicana* ICP with an N-terminal 6XHis-tag were used in these experiments. Each plasmid encodes for a double mutant to produce a protein with a single cysteine residue: (1) C56S, K27C (ICP K27C) and (2) C56S, K8C (ICP K8C). C41 (DE3) *E. coli* cells were transformed with each plasmid and grown in 1 L of LB media with 50 µg/mL kanamycin at 37 °C until an optical density at 600 nm of 0.6-0.8 was reached. The culture was induced with 1 mL of 1 M IPTG and grown at 17 °C for 20 h. The cells were harvested and lysed using 1 mL BugBuster in 10 mL lysis buffer (10 mM Tris, 150 mM NaCl, 10 mM imidizole, pH 7.5) and sonication on ice (3 iterations of a 30/10 seconds on/off pulse cycle at 40% power). Cleared lysate was obtained by centrifugation at 30,000g for 30 min at 4 °C, and the protein was purified by Ni-affinity chromatography. A 2 mL column bed of Ni Sepharose Fast Flow was equilibrated with 4 mL 20 mM sodium phosphate, 500 mM sodium chloride, 20 mM imidazole at pH 7.4. The cleared lysate was loaded onto the column and washed with 8 mL of the same equilibration buffer. The protein was eluted with 4 x 2 mL of 20 mM sodium phosphate, 500 mM sodium chloride, 500 mM imidazole at pH 7.4, and further purified by gel filtration

chromatography using a Hiprep 26/60 Sephacryl S-100 column and 20 mM potassium phosphate, 150 mM NaCl buffer at pH 7.2. The protein elution was collected and analyzed using SDS-PAGE to confirm the purity and identity of the protein. To reduce disulfide bonds that commonly form between monomers of ICP, 5 mM TCEP was added to the stock solution. Excess TCEP was removed by buffer exchange into SPR buffer (100 mM sodium phosphate and 100 mM sodium chloride at pH 7.0) using a 5 kDa molecular-weight cut-off centrifugal filter before SPR analysis.

2.4. Purification of Papain for SPR

Due to impurities in the papain stock detected by SDS-PAGE, steps were taken to purify stock solutions of papain before use. A fresh solution of 5 mg/mL papain (Sigma-Aldrich, Cat # P4762, Lot # SLBC2123V) in water was prepared. A 1 mL injection was purified by gel filtration using a Sephadex G50-medium (4 mL) column at a flow rate of 5 mL/min. The run buffer used was 100 mM sodium phosphate and 100 mM sodium chloride at pH 7.0. The final concentration was determined using the Bio-Rad Coomassie Assay following the manufacturer's instructions.

2.5. Reductive Methylation of Papain

Stock solutions of 1 M dimethylamine borane (DMAB) and 1 M formaldehyde were prepared fresh before each reaction. An aliquot of DMAB equal to 10x molar excess of lysine residue concentration (papain contains 11 lysine residues) was added to the papain stock solution. Immediately, an aliquot of formaldehyde equal to 20x molar excess of lysine residue was added. The reaction mixture was protected from light with aluminum foil and allowed to react for 2 hours at 4 °C with constant gentle mixing. This step was repeated with another aliquot each of DMAB and formaldehyde. A final aliquot of DMAB was added, and the reaction

11

mixture was left for 20 hours at 4 °C with constant gentle mixing. An aliquot of 125 µL of 10 mM ammonium sulfate was added to quench the reaction. The reductively methylated papain was exchanged into SPR run buffer (100 mM sodium phosphate and 100 mM sodium chloride at pH 7.0) using a 5 kDa molecular-weight cut-off centrifugal filter for binding kinetics analysis.

2.6. Study of Papain-ICP Interaction with SPR

All SPR studies were performed using a Biacore X100 (GE Healthcare). For binding and kinetics assays, the run buffer used was 100 mM sodium phosphate, 100 mM sodium chloride, pH 7.0 (flow rate 5 µL/min). A linear polycarboxylate hydrogel chip modified with nitrilotriacetic acid (NTA) was regenerated with a solution of 0.35 M ethylenediaminetetraacetic acid (EDTA) and then treated with a solution of 5 mM nickel chloride to complex Ni^{2+} ions with the surface. The ICP mutant of choice (K8C or K27C) was immobilized on the chip channel 2 at the N-terminal 6x histidine tag (his-tag) by washing the chip with a solution of 100 µg/mL of reduced ICP mutant in immobilization buffer (10 mM HEPES, 0.005% Tween 20, 0.15 M NaCl, and 5 µM EDTA, pH 8.5). A simplified visual of this procedure is shown in Figure 2.1. The sensor chip was regenerated in order to immobilize fresh ICP on the surface before each experiment.
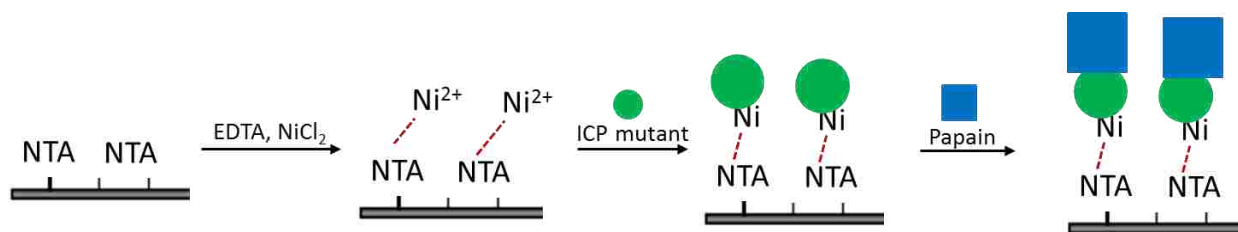
Figure 2.1: A visual representation of the chip surface. An NTA-modified polycarboxylate hydrogel chip is modified with nickel ions in order to immobilize ICP by its N-terminal his-tag. The immobilized ICP is then available for papain binding for kinetics studies.

The single-cycle kinetic approach was used with varying concentrations of papain in run buffer to produce a binding curve for kinetics assays, and to determine the dissociation constant

(K_D) for the protein-protein interaction using the association and dissociation rate constants (k_a and k_d, respectively) determined for papain and ICP. All data were analyzed using a 1:1 binding model using the evaluation software provided by GE Healthcare. The formula for the determination of K_D from k_d and k_a uses the following equation:

$$K_D = \frac{k_d}{k_a}$$

2.7. Results

Attempts to immobilize the K8C mutant of ICP to the sensor chip surface were unsuccessful. No increase in the SPR signal baseline was observed after multiple attempts, including attempts with modified immobilization conditions. It is possible that ICP K8C is susceptible to protease cleavage of its N-terminus, which would remove the 6x his-tag and prevent immobilization. Another possibility is that the N-terminus is buried in the structure and sterically hindered from immobilization. Since the K8C mutant could not be anchored to the sensor chip, it was not possible to determine kinetic data for the interaction between papain and ICP K8C. SPR studies with ICP K8C were discontinued. An example of a reference-subtracted sensorgram for these attempts can be seen in Figure 2.2.
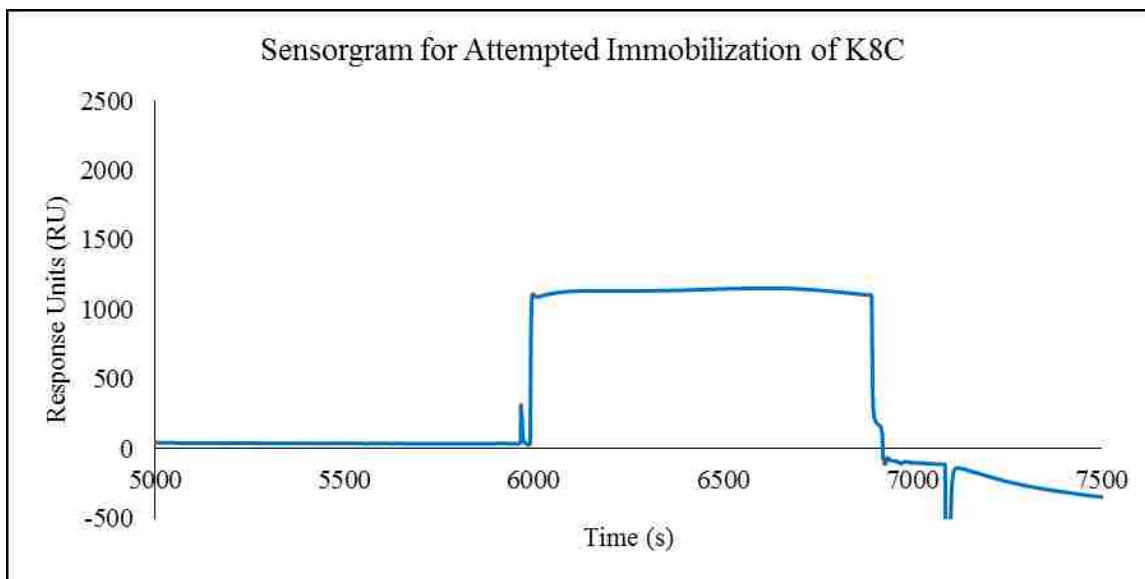
Figure 2.2: Reference-subtracted sensorgram for the attempted immobilization of K8C on a Ni-NTA modified SPR sensor chip. Time 6000 s marks the beginning of the flow of immobilization buffer containing the K8C mutant, until 6900 s.
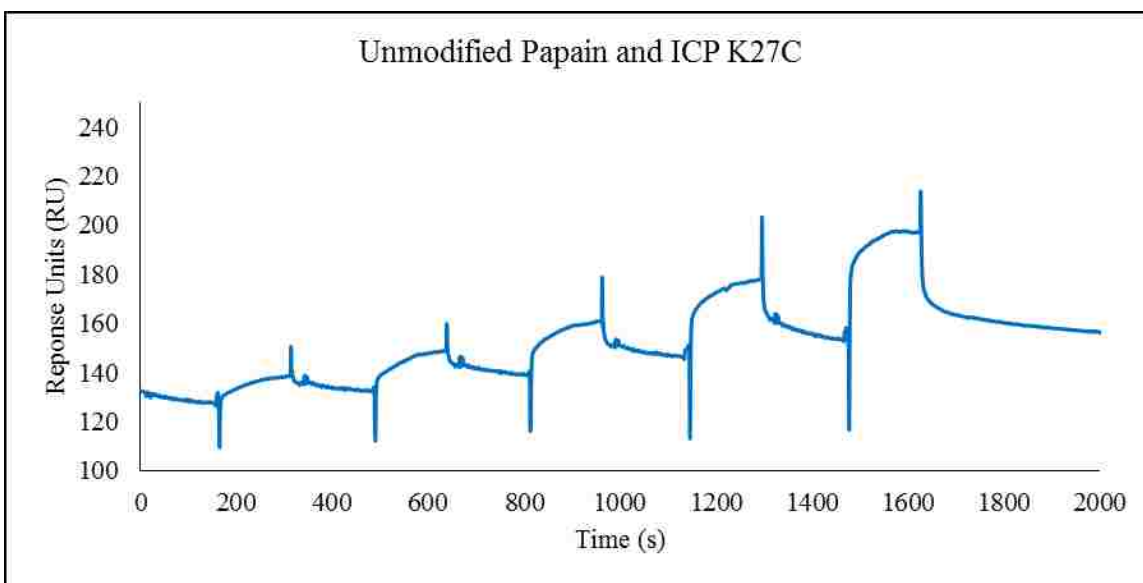
Figure 2.3: Reference-subtracted sensorgram for the interaction of unmodified papain with immobilized ICP K27C. The concentrations of papain used for this trial were 50, 100, 200, 400, and 800 nM.
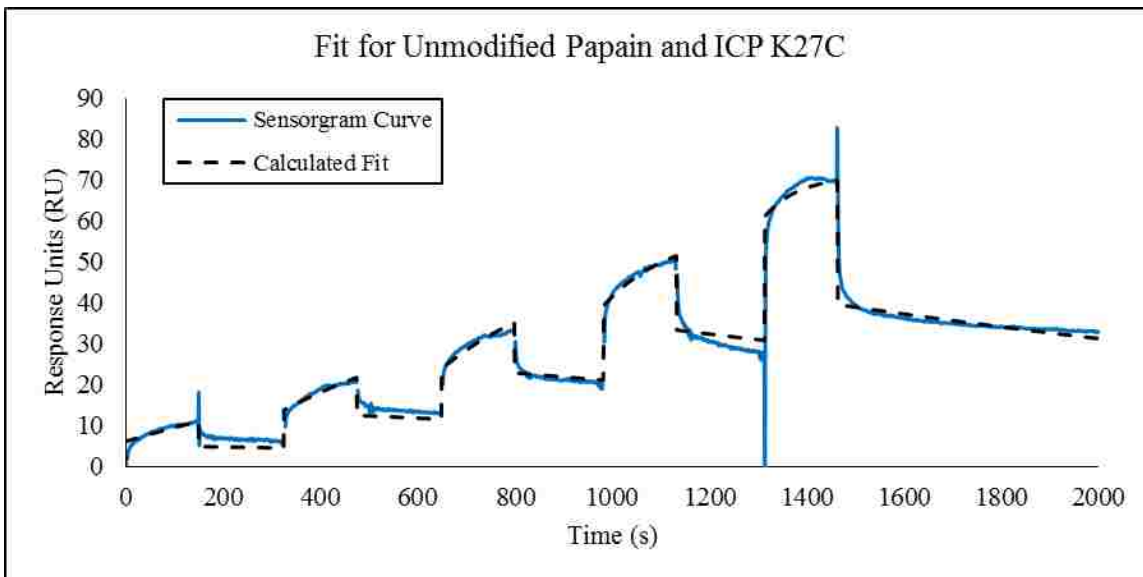
Figure 2.4: Blank-subtracted and reference-subtracted sensorgram used by the Biacore software to determine kinetic data for unmodified papain and ICP K27C. The solid blue line represents the sensorgram. The dashed black line is the best fit to a 1:1 binding model. "Spikes" in the sensorgram produced by bulk effects were removed manually before the determination of the fit.

Immobilization of ICP K27C was successful. Single-cycle kinetic analysis using 50, 100, 200, 400, and 800 nM of papain was performed. The blank-subtracted sensorgram is shown in Figure 2.3. The sensorgram curve was fit using a 1:1 binding model using the evaluation software on the Biacore X100. The data and the fit are shown in Figure 2.4. The equilibrium dissociation constant (K_D) was determined to be 25.7 nM.

Binding of RM-papain to mounted K27C was also successful. The data was fit to a 1:1 binding model using the evaluation software, and the K_D for the interaction was determined to be 9.4 nM. The blank-subtracted sensorgram is shown in Figure 2.5, and the calculated fit is shown in Figure 2.6.

Table 1 contains a list of the calculated K_D values for each mutant interaction with unmodified papain or RM-papain. Data for the E102C mutant was determined previously by Pamlea Brady and is included with permission.

Table 1. Overview of Papain-ICP Binding Data	
Mutant + Papain	K_D
K8C + unmod. papain	--
K27C + unmod. papain	25.7 ± 0.9 nM
K27C + RM-Papain	9.4 ± 0.9 nM
E102C + RM-papain [*]	4 ± 1 nM

* = Data from Pamlea Brady's dissertation, provided for comparison. Reprinted with permission.
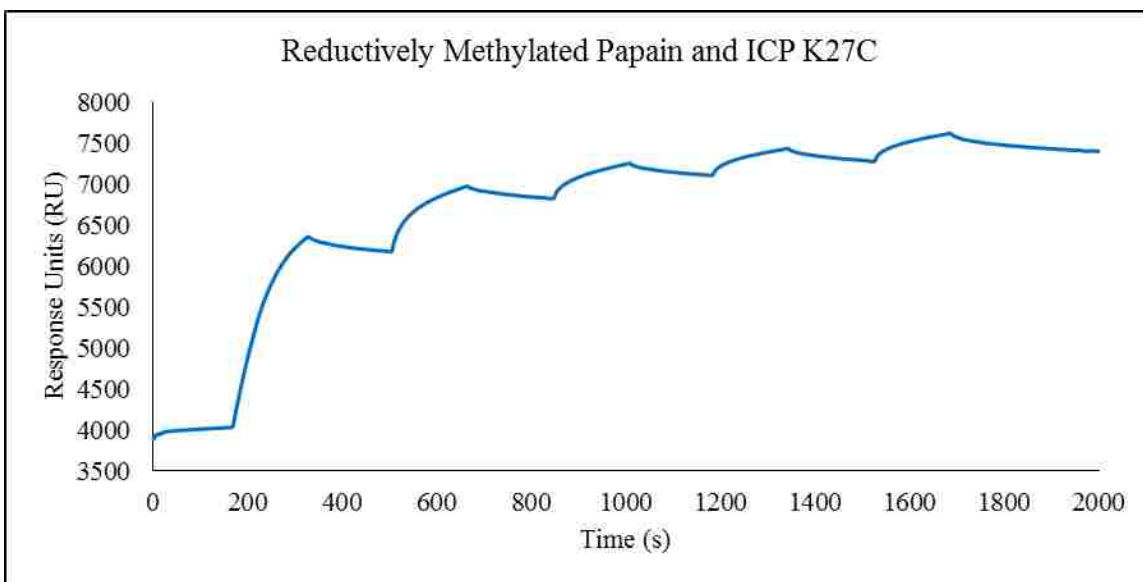
Figure 2.5: Reference-subtracted sensorgram for the interaction of RM-papain with immobilized ICP K27C. The concentrations of papain used for this trial were 200, 400, 600, 800, and 1000 nM.
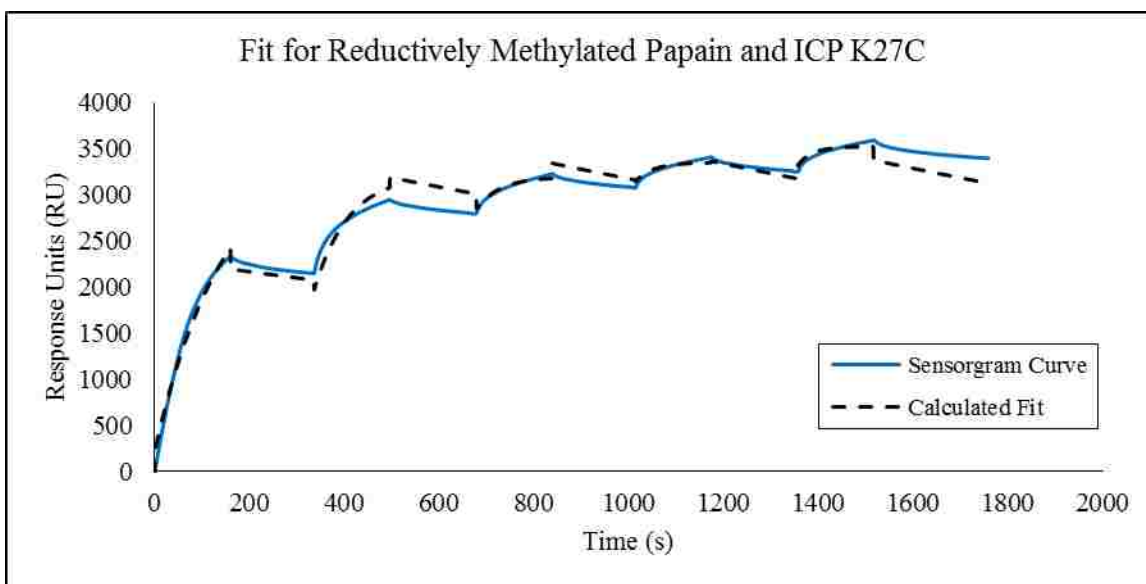
Figure 2.4: Blank-subtracted and reference-subtracted sensorgram used by the Biacore software to determine kinetics data for RM-papain and ICP K27C. The solid blue line represents the sensorgram. The dashed black line is the fit that the software calculated and used to determine the K_D value of the interaction. "Spikes" in the sensorgram produced by bulk effects were removed manually before determination of the fit.

2.8. Discussion

Unique K_D values were determined for ICP K27C with unmodified papain and with RM-papain. The determined constants are both in the nanomolar range, which is consistent with

16

previous studies (4,5) and indicates a tight-binding and favorable interaction. Since there is no significant difference in these values, we can conclude that the methyl groups introduced at the lysine residues of papain do not interfere with papain-ICP binding. This observation is further confirmed when comparing these data with data collected from previous experiments by Pamlea Brady, which showed that the interaction between ICP mutant E102C and RM- papain has a K_D in the nanomolar range as well.

The errors reported in Table 1 were determined from the calculated fit using the Biacore software. This error does not include any error that could arise from measuring the protein concentration using the Coomassie assay or making low-concentration solutions of proteins in buffer. These sources of error are expected to be larger than the fit error; hence, the values of 25.7 nM, 9.4 nM, and 4 nM are not significantly different. Moreover, if methylation did interfere with binding, we would expect to see a 1000+ fold change in K_D.

2.9. Conclusion

Reductive methylation of proteins is a common method for the introduction of methyl groups for NMR and x-ray crystallographic studies (6). However, any modifications of proteins may inhibit or prevent complex formation. In order to study the papain-ICP complex with reductively methylated papain, it is necessary to ensure that binding still occurs. The SPR studies in this chapter resulted in K_D values in the nanomolar range, and with no significant difference between those experiments using unmodified papain and RM-papain. These data show that complex formation is tight-binding and favorable between ICP and papain, and that the methyl groups of RM-papain do not interfere with its ability to bind with ICP. When ^{13}C formaldehyde is used to add ^{13}C-labeled methyl groups to the lysine residues of papain, NMR studies of the papain-ICP complex can be performed.

The SPR method used in this study allowed us to collect unique data for reductively methylated papain and successfully determine if this modification interferes with the protein's ability to complex with our ICP mutants. This method can also be used for the screening of mutants with decreased binding with papain. If the ability of an ICP mutant to bind with papain has been compromised, SPR can be used to identify this and eliminate it from future studies.

2.10. References

1.   Mitchel, R. E., Chaiken, I. M., and Smith, E. L. (1970) The complete amino acid sequence of papain. Additions and corrections. *J. Biol. Chem.* **245**, 3485-3492

2.   Besteiro, S., Coombs, G. H., and Mottram, J. C. (2004) A potential role for ICP, a leishmanial inhibitor of cysteine peptidases, in the interaction between host and parasite. *Mol. Microbiol.* **54**, 1224-1236

3.   Sanderson, S. J., Westrop, G. D., Scharfstein, J., Mottram, J. C., and Coombs, G. H. (2003) Functional conservation of a natural cysteine peptidase inhibitor in protozoan and bacterial pathogens. *FEBS Lett.* **542**, 12-16

4.   Muehlenweg, B., Assfalg-Machleidt, I., Parrado, S. G., Burgle, M., Creutzburg, S., Schmitt, M., Auerswald, E. A., Machleidt, W., and Magdolen, V. (2000) A novel type of bifunctional inhibitor directed against proteolytic activity and receptor/ligand interaction. Cystatin with a urokinase receptor binding site. *J. Biol. Chem.* **275**, 33562-33566

5.   Chhikara, N., Saraswat, M., Tomar, A. K., Dey, S., Singh, S., and Yadav, S. (2012) Human Epididymis Protein-4 (HE-4): A Novel Cross-Class Protease Inhibitor. *PLoS ONE* **7**, e47672

6.   Hattori, Y., Furuita, K., Ohki, I., Ikegami, T., Fukada, H., Shirakawa, M., Fujiwara, T., and Kojima, C. (2013) Utilization of lysine (1)(3)C-methylation NMR for protein-protein interaction studies. *J. BIol. NMR* **55**, 19-31

CHAPTER 3: STRUCTURE ELUCIDATION OF THE PAPAIN-ICP COMPLEX USING PARAMAGNETIC RELAXATION ENHANCEMENT NMR

3.1. Introduction

Although a model exists for the papain-ICP complex, based on chemical shift perturbations in NMR spectra when ICP is bound to papain, it is largely supplemented by information derived from the binding of papain with a different cysteine protease inhibitor, stefin B (1). Due to the lack of information concerning specific interactions between ICP and papain, the full structure of the papain-ICP complex has yet to be solved. Our goal is to improve the existing model, or to propose a new model of the complex. This model will include information about specific dimensions of the proteins that can be determined through paramagnetic relaxation enhancement (PRE) NMR studies.

In the work detailed in this chapter, PRE-NMR was used to determine intermolecular distances between residues of ICP labeled with paramagnetic tags and ^{13}C-enriched reductively methylated lysine residues of papain when the two proteins form a complex. These distances were used to create a new preliminary working model for the papain-ICP complex. Electron paramagnetic resonance spectroscopy was used to determine the percent of ICP successfully labeled with the paramagnetic tag used.

3.1.1. Using NMR to Study Protein Complexes

The study of proteins and protein structure using NMR has become a very broad field since its beginnings in the 1980s (2). There are many established methods for the determination of protein structure, covering everything from backbone structure and side chain analyses, to distance and dynamic measurements (3). Furthermore, methods have been developed to study protein complexes in solution, providing more information about two or more proteins at once – specifically, their quaternary structure, or how the proteins interact with each other (4). These

advances have made NMR structural determination of proteins an integral part of analytical and biochemical fields of study.

One method for studying proteins with NMR is a technique called reductive methylation. Reductive methylation is a highly selective reaction that adds two methyl groups to the side chains of lysine residues as well as the α-amino group of the *N*-terminus. It does not alter the pI of the protein, nor does it disrupt the positive charge of the lysine side chain (5). It is commonly known as a routine "rescue strategy" in protein crystallization studies, as the reductive methylation of proteins has proven to increase the degree of successful crystallization for analysis (6). This technique can be applied to NMR structural studies through the addition of ^{13}C-enriched methyl groups, which label the protein at known positions. There have been many studies reported that take advantage of ^{13}C-enriched reductive methylation for the study of intramolecular distances of proteins, (7-9) as well as intermolecular distances between complexed proteins (10-12). Although these distance constraints are sparse, the data can be useful for determining the quaternary structure of protein-protein interactions and complex formations.

3.1.2. Paramagnetic Relaxation Enhancement NMR in Protein Complex Analysis

In PRE-NMR, a paramagnetic label is attached to a known site on a protein. This technique is called site-directed spin labeling, and it has been previously used to study interactions between proteins in solution using NMR. (13-15) A common label used for site-directed spin labeling is *S*-(1-oxyl-2,2,5,5-tetramethyl-2,5-dihydro-1H-pyrrol-3-yl)methyl methanesulfonothioate (MTSL), which is attached to a cysteine residue of a protein. This reaction is shown in Figure 3.1.

When a paramagnetic label is present, the relaxation rate of nearby nuclei is increased. In NMR spectra, this rate increase causes peak perturbation: broadening of the peak is increased and the intensity of the peak decreases. The degree of peak perturbation as compared to the peak in its unaffected form is related to the distance (r) of the affected nucleus from the paramagnetic label by the relationship: $1/r^6$. Using this relationship, distances of up to 35 Å can be measured. This method can be used to measure much longer distance constraint than methods based on the nuclear Overhauser effect (NOE), which can detect distances up to 6 Å. This long-range measurement capability makes PRE-NMR an appealing candidate for the analysis of protein complexes.
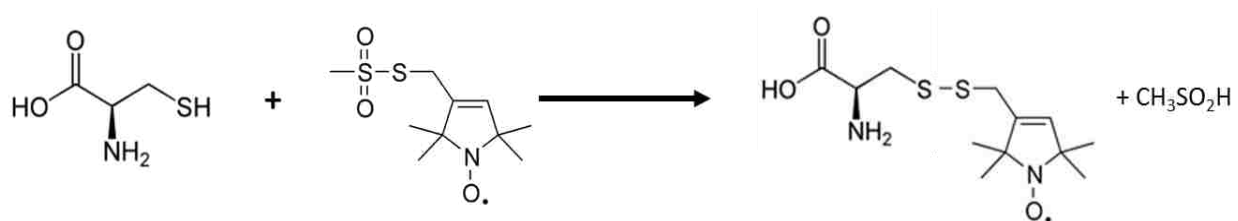
Figure 3.1: A chemical formula representing the attachment of the MTSL label to a cysteine. A disulfide bond is formed between the available thiol of the cysteine and the thiol of the label.

3.2. Materials

Two pET28 plasmids encoding *Leishmania mexicana* ICP with an N-terminal 6XHis-tag was supplied by Brian O. Smith, University of Glasgow, Glasgow, UK. Papain from papaya latex (*Carica papaya*), isopropyl β-D-1-thiogalactopyranoside (IPTG), kanamycin, (tris(2-carboxyethyl)phosphine) (TCEP), imidazole, succinic acid (succinate), sodium chloride (NaCl), sodium phosphate monobasic, potassium phosphate monobasic, potassium phosphate dibasic, dimethylamine borane (DMAB), tris(hydroxymethyl)aminomethane (tris), formaldehyde, ^{13}C-formaldehyde solution, glycine, ethanol, and methanol were purchased from Sigma-Aldrich. Luria broth (LB) media was purchased from Fisher Scientific. BugBuster 10x concentrated lysis buffer solution was purchased from EMD Millipore. Ni Sepharose Fast Flow media was

purchased from GE Healthcare Sciences. S-(1-oxyl-2,2,5,5-tetramethyl-2,5-dihydro-1H-pyrrol-3-yl)methyl methanesulfonothioate (MTSL) was purchased from Toronto Research Chemicals. All water used was taken from a Millipore Direct-Q3 water system by EMD Millipore.

3.3. Expression and Purification of *L. mexicana* ICP Mutants

Mutants of *L. mexicana* ICP were expressed using the same protocol as in Chapter 2 of this dissertation, Section 2.3. The mutants used in these NMR studies were (1) C56S, K27C (ICP K27C) and (2) C56S, E102C (ICP E102C).

3.4. Spin Labeling of ICP

The single cysteine-ICP mutants have been shown to form disulfide bonds between monomers, creating dimers that are unsuitable for protein complex studies. In order to ensure that all ICP in solution is in monomer form, it was necessary to reduce any existing disulfide bonds between ICP monomers. A 15x molar excess of tris(2-carboxyethyl)phosphine (TCEP) was added to stock solutions of ICP mutants and was allowed to react at room temperature for 10 mins. The samples were immediately desalted by exchanging the buffer to NMR buffer (20 mM succinate, 50 mM NaCl, pH 5.0) using 5 kDa molecular-weight cut-off centrifugal filters at 5,000 x g to remove excess TCEP. A 20x molar excess of the spin label (MTSL) was added to the ICP samples and allowed to react for 15 hrs at 4 °C while protected from light. Unreacted MTSL was removed from the protein by exchanging the buffer to succinate buffer as before.

3.5. Reductive Methylation of Papain

Papain was reductively methylated (RM-papain) using the protocol explained in Chapter 2 of this dissertation, Section 2.5. ^{13}C-enriched formaldehyde was used for the addition of ^{13}C

labeled methyl groups. NMR buffer (20 mM succinate, 50 mM NaCl, pH 5.0) was used for all experiments.

3.6. Instrumentation

The purpose of these studies was to use PRE-NMR to measure specific distances between papain and ICP when a complex is formed. 2D NMR experiments were performed to compare the intensity of ^{13}C-methyl peaks from RM-papain that are near the paramagnetic labels on MTSL-labeled ICP (MTSL-ICP) to their intensity when the paramagnetic labels are reduced. In order to take advantage of relaxation enhancement of ^{13}C-methyl peaks, it is important to confirm that ICP is sufficiently labeled with the MTSL tag. Electron paramagnetic resonance (EPR) was used to determine the percent of ICP labeled with MTSL.

3.6.1. EPR of ICP for Determination of Percent of Sample Labeled

Experiments were performed on a Bruker EMX-20/2.7 spectrometer equipped with a dual cavity probe at room temperature. Parameters were adjusted manually to produce the best possible spectra going forward. The microwave frequency was 9.789 GHz and the power was 19.84 mW. Sweep time was set to 168 s, conversion time was 163.8 ms. The time constant was 40.96 ms. Modulation patterns consisted of 1024 data points for data collection and processing.

MTSL calibration standards at concentrations of 1, 3, 5, 7, 9, and 10 µM in succinate buffer (20 mM succinate, 50 mM NaCl, pH 5.0) were made from a stock solution of 37.8 µM MTSL in acetonitrile. A calibration curve was formed by plotting the value of the 2nd integration of the spectra (determined with the on-system evaluation software WINEPR provided by Bruker) versus the concentration of the standard. Linear least squares regression was used to determine the line of best fit. MTSL-ICP samples were analyzed, and the calibration curve was used to determine the concentration of MTSL present in the sample. This value was compared to the

known ICP concentration of the sample, as determined by the Coomassie assay, to determine the percent of ICP labeled with MTSL.

3.6.2. NMR Analysis of the Papain-ICP Complex

NMR samples were made to a volume of 500 µL with a molar ratio of 1:1 MTSL-ICP to RM-papain. 2D ^{1}H-^{13}C heteronuclear single quantum coherence (HSQC) spectra were acquired on a 700 MHz Varian spectrometer with a 5 mm HCN probe at room temperature. All experiments were collected with 8 scans and a relaxation delay of 5 s. The total experiment time was 5 hrs and 35 mins.

After acquiring spectra for samples while the MTSL label was in its paramagnetic (oxidized) form, the label was reduced with an addition of 5 mM sodium ascorbate. In its reduced state, the MTSL label was diamagnetic ("inactive"), and another experiment was run using the same parameters. The spectra were compared for any evidence of peak perturbations. All spectra were processed using NMRpipe (16) and visualized with NMRview (17).

3.7. Results

EPR analysis of MTSL-ICP samples and MTSL standards produced the expected spectra. Three peaks were observed at even intervals. The second derivative of these spectra were calculated, and the area under the curve was used for concentration determination. An example of a calibration curve used is shown in Figure 3.2. The average percent labeling of the MTSL-ICP sample was found to be 82% for the E102C mutant, and 80% for the K27C mutant.
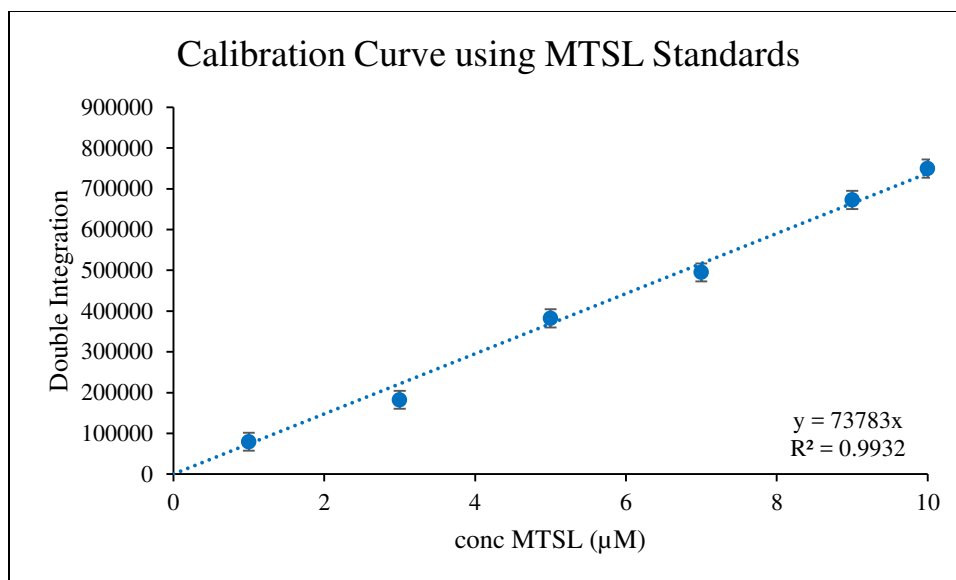
Figure 3.2: An example of a calibration curve used to determine the percentage of ICP in solution labeled with the MTSL paramagnetic tag.

NMR spectra of ICP K27C in complex with RM-papain before and after the reduction of the MTSL spin label on ICP K27C are overlaid in Figure 3.3. All peaks are perturbed to some degree when the MTSL label is paramagnetic. Of note, peak 11 is no longer present in the paramagnetic MTSL sample. It is also notable that peaks $4 - 6$ show a significant decrease in intensity when the MTSL label is paramagnetic.
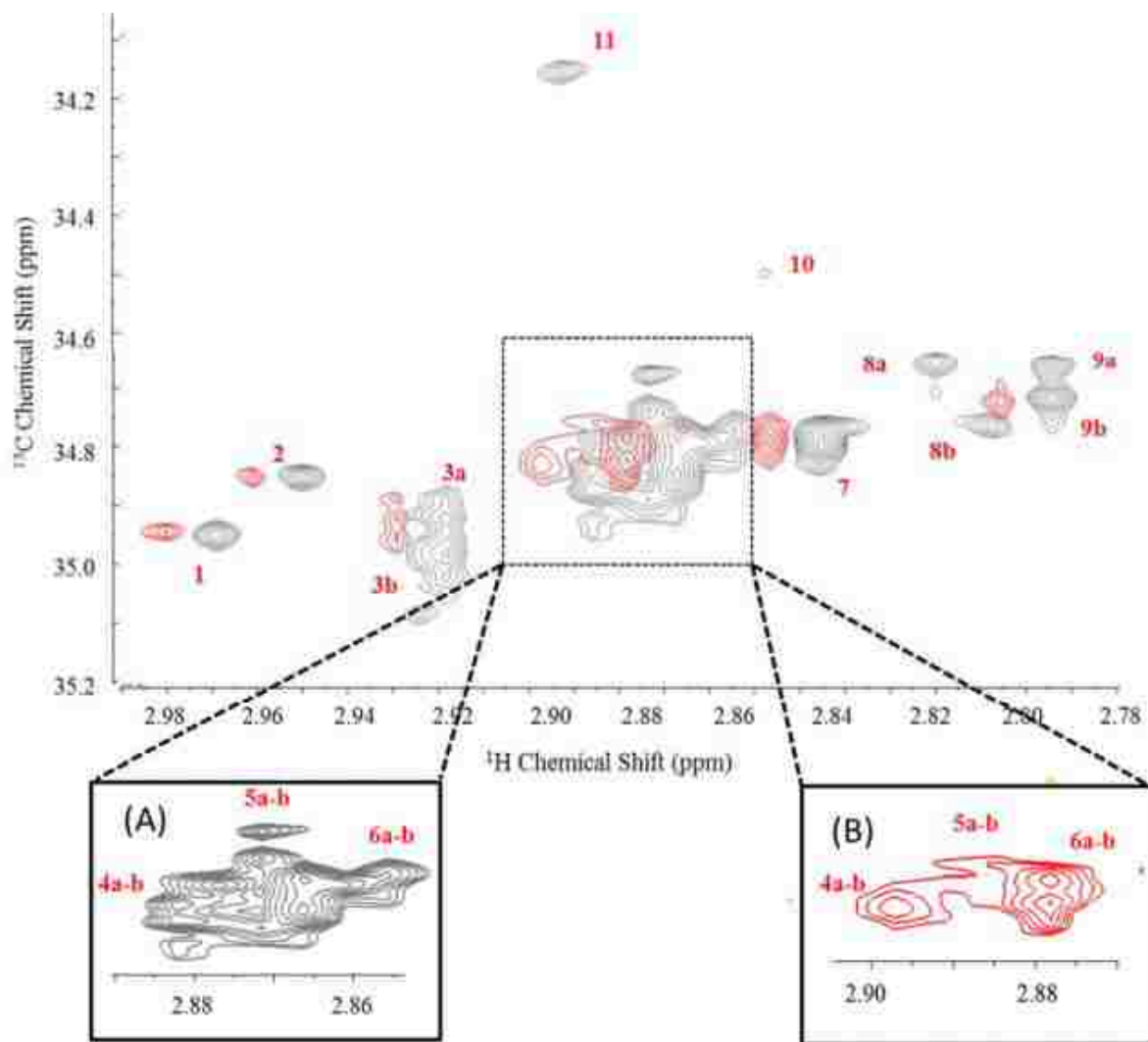
Figure 3.3: Overlay of spectra for the complex of papain and ICP-K27C with MTSL (red), and of the same complex after MTSL has been reduced. Spectra are offset along the x-axis to for the comparison of peak intensities. Boxes (A) and (B) show a zoom of the central area of the spectra, separated for easier viewing.

Spectra of the RM-papain and ICP E102C complex before and after the reduction of the MTSL label on ICP E102C were overlaid in Figure 3.4. Here, we observe less overall peak perturbation across the spectra, when we compare the results to the ICP K27C sample. Only peaks 4a and 4b appear to have decreased in intensity in the presence of the paramagnetic label, and even that amount is not as significant as the decreases in intensity with the ICP K27C sample.
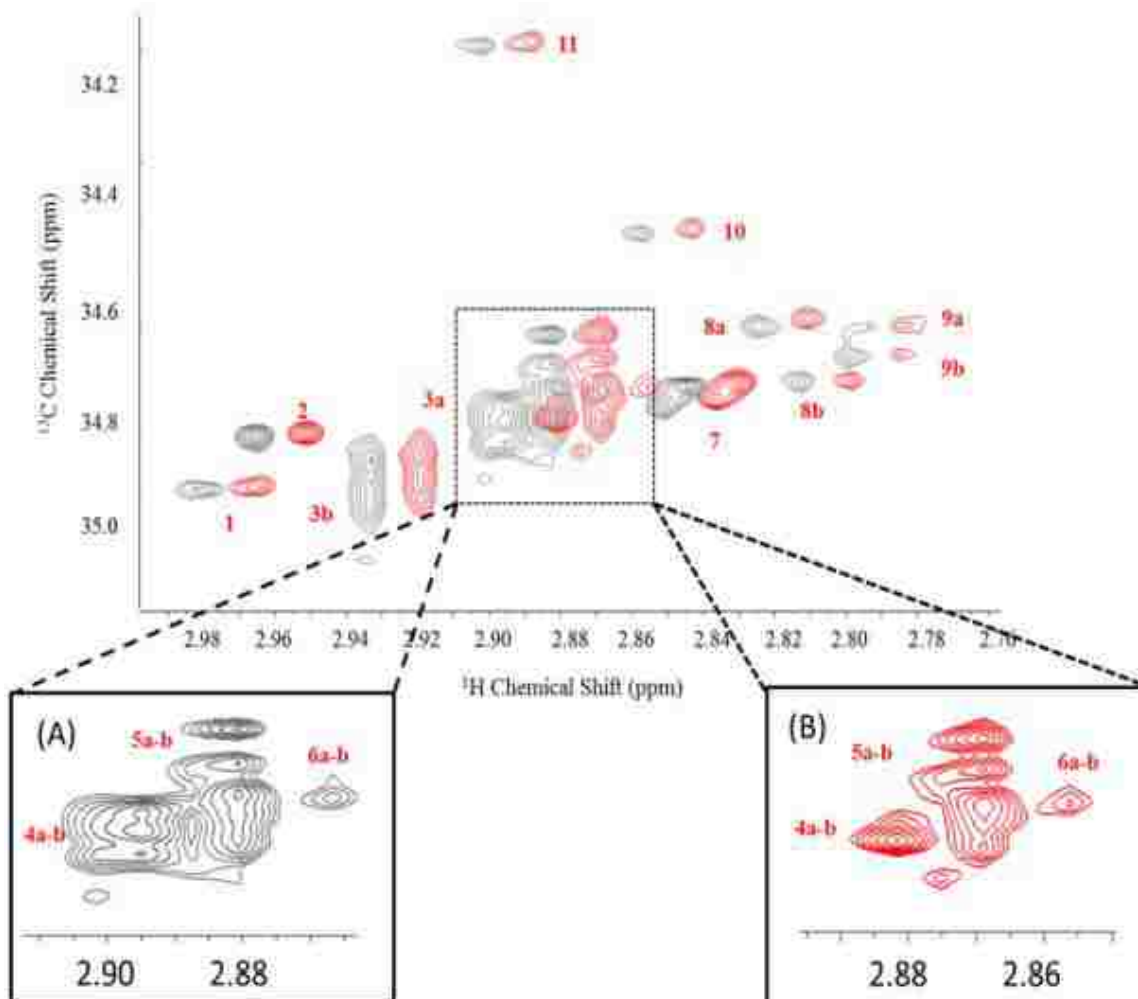
Figure 3.4: Overlay of spectra for the complex of papain and ICP-E102C with MTSL (red), and of the same complex after MTSL has been reduced. Spectra are offset along the x-axis to for the comparison of peak intensities. Boxes (A) and (B) show a zoom of the central area of the spectra, separated for easier viewing.

3.8. Discussion

The disappearance of peaks in the presence of the MTSL label on ICP K27C indicate that those lysine residues of papain are well within the 35 Å range of residue 27 of ICP. With such a high degree of perturbation, these lysine residues must be close enough to experience significant relaxation enhancement. Since other peaks were perturbed, especially peaks 4 − 6, position 27 of ICP must be near to all of them. This observation is significant information for the development of our model. It is possible that position 27 is close to, if not well within, the catalytic cleft of

papain when the complex is formed. This scenario positions ICP in a way that most – if not all – of the lysine residues of papain are within range of relaxation enhancement.

The NMR spectra of the E102C mutant complexed with papain had significantly fewer instances of peak perturbation. Only peaks 4a and 4b show any signs of relaxation enhancement due to the MTSL label. From this, we can assume that residue 102 of ICP is far from papain even when the complex is formed, and that only a single methyl group – a single papain lysine – is close to this residue.
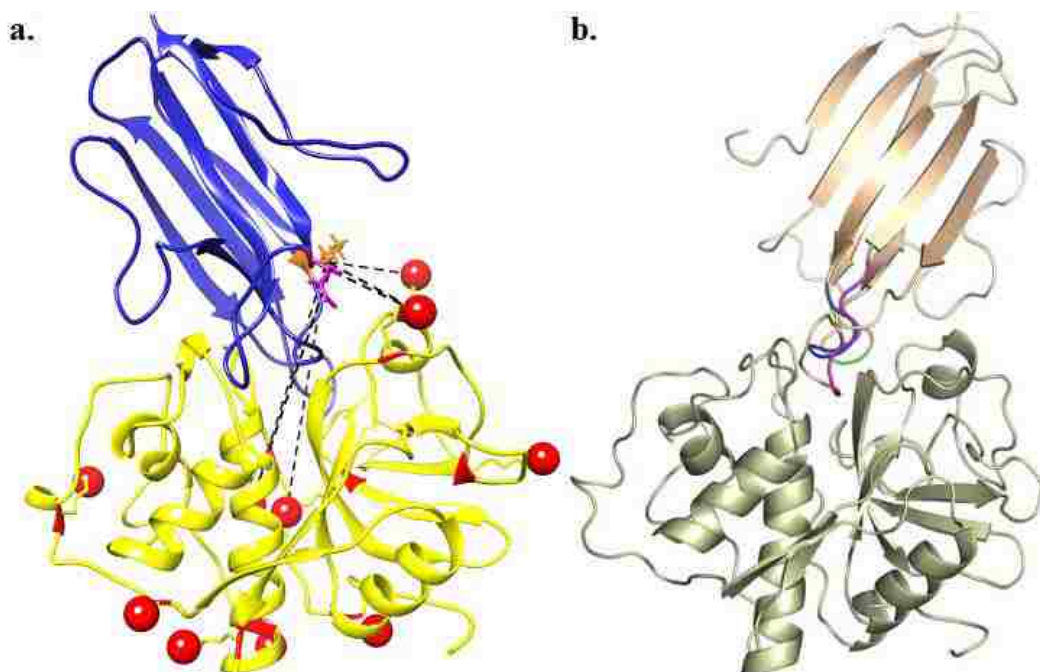
Figure 3.5: a. Our proposed model, created in USCF Chimera software, using information from PRE-NMR studies. b. The complex model proposed by Smith, et al. (1), used with permission.

Using the information from the PRE-NMR studies, a model was developed by positioning known, individual structures of ICP and papain in proximity to each other to simulate complex formation. Distances were calculated using the modeling software, and the model was adjusted to best represent the position of methylated lysines in relation to the positions where the MTSL tags were located. Figure 3.5a shows a full image of the model developed. For a side-by-side comparison, the model created by Smith et al. is provided as well (Figure 3.5b) (1).

Compared to Smith's model, ICP is rotated nearly 180 degrees. This reverses the positions of the three binding loops of ICP, placing the outer loops at opposite ends of the catalytic cleft. The chemical shift perturbations observed by Smith *et al.* are consistent with our model as the loops maintain contact with the catalytic cleft. Additionally, we see that residues 27 and 102 are in different locations. Residue 27 is now closer to papain lysines 139 and 156 in particular and is within 35 Å of others. In Smith's model, residue 102 does not appear to be within range of any lysines. Our model accounts for the interaction of residue 102 with a single methyl group at lysine 156. A zoom view of the binding site between ICP and papain is shown in Figure 3.6. Residue 27 of ICP is well within the 35 Å range of surrounding papain lysines, while residue 102 is outside of this range for all but one methyl group on lysine 156.
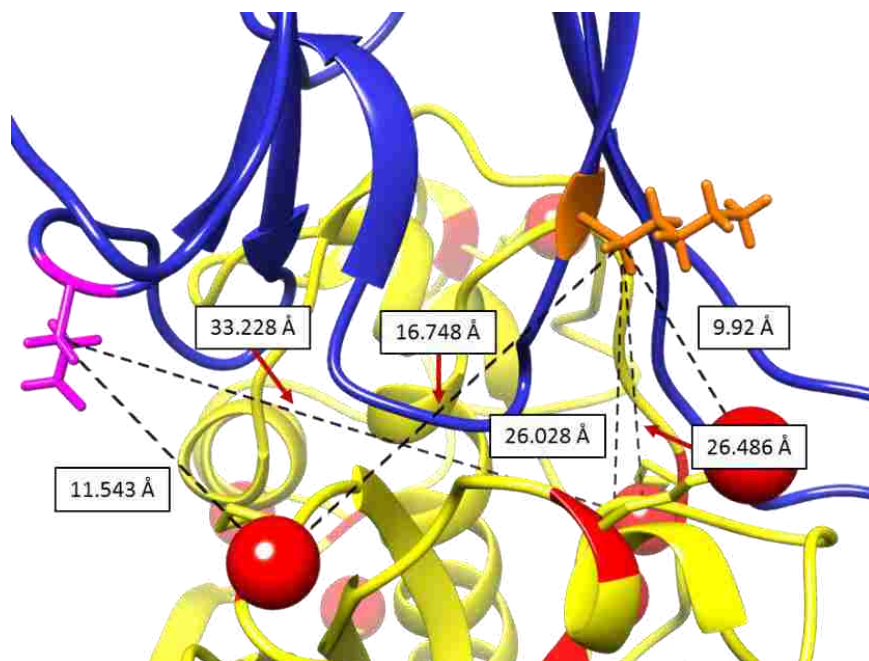
Figure. 3.6: Close-up view of the binding site between ICP and papain. The 27 position (orange) and the 102 position (pink) of ICP are highlighted. Lysine side-chains of papain are displayed as red spheres. Distances were determined using chimera software.

3.9. Future Work

The model proposed in this dissertation is an improvement on the available model of papain-ICP. It takes into account specific distances between lysine residues in papain and

cysteine residues at different locations in mutants of ICP. However, it is still not a perfected model, and further study is necessary to calculate more distances and refine the model. Other MTSL-labeled mutants of ICP can be used to cover other distance determinations and give insight into specific interactions between ICP and papain during complex formation.

Distance calculations are complicated by the flexibility of the lysine side-chains. Behavior of the protein in solution means that the ^{13}C-methyl groups on the lysines are not always in the same place. Because of this uncertainty, our model is based on qualitative data rather than calculated distances. However, with enough data collected, an average could be used to determine distance constraints related to the PRE effects using the relationship described by $1/r^6$. With these distances constraints and the chemical shift perturbations, computational docking experiments could be used to improve the model of the complex.

3.10. Conclusion

PRE-NMR was used to study the structure of the papain-ICP complex. ICP mutants with a single cysteine residue in different locations were labeled with the paramagnetic tag, MTSL. When in close proximity to ^{13}C-enriched methyl groups attached to lysine residues on papain, the corresponding NMR peaks were perturbed. The higher the amount of perturbation, the closer the lysine residue must be to the position of the MTSL tag. Using information obtained from the mutants K27C and E102C of ICP, a new model of the complex was created.

Future work will involve repeating the method with other mutants of ICP, allowing for more determinations of distances between papain lysines and corresponding ICP residues. It will be necessary to account for the flexibility of lysine side-chains in order to determine distances accurately. With more distance constraints determined and more information about the

interactions of the two proteins, the full structure of the papain-ICP complex can be modeled confidently.

3.11. References

1.   Smith, B. O., Picken, N. C., Westrop, G. D., Bromek, K., Mottram, J. C., and Coombs, G. H. (2006) The structure of *Leishmania mexicana* ICP provides evidence for convergent evolution of cysteine peptidase inhibitors. *J. Biol. Chem.* **281**, 5821-5828

2.   Kay, L. E. (1997) NMR methods for the study of protein structure and dynamics. *Biochem. Cell Biol.* **75**, 1-15

3.   Kay, L. E. (2005) NMR studies of protein structure and dynamics. *J. Magn. Reson.* **173**, 193-207

4.   Wand, A. J., and Englander, S. W. (1996) Protein complexes studied by NMR spectroscopy. *Curr. Opin. Biotech.* **7**, 403-408

5.   Means, G. E., and Feeney, R. E. (1968) Reductive alkylation of amino groups in proteins. *Biochemistry* **7**, 2192-2201

6.   Walter, T. S., Meier, C., Assenberg, R., Au, K. F., Ren, J., Verma, A., Nettleship, J. E., Owens, R. J., Stuart, D. I., and Grimes, J. M. (2006) Lysine methylation as a routine rescue strategy for protein crystallization. *Structure* **14**, 1617-1622

7.   Gerken, T. A., Jentoft, J. E., Jentoft, N., and Dearborn, D. G. (1982) Intramolecular interactions of amino groups in 13C reductively methylated hen egg-white lysozyme. *J. Biol. Chem.* **257**, 2894-2900

8.   Abraham, S. J., Cheng, R. C., Chew, T. A., Khantwal, C. M., Liu, C. W., Gong, S., Nakamoto, R. K., and Maduke, M. (2015) 13C NMR detects conformational change in the 100-kD membrane transporter ClC-ec1. *J. Biomol. NMR* **61**, 209-226

9.   Szasz, J., Yaffe, M. B., and Sternlicht, H. (1993) Site-directed mutagenesis of alpha-tubulin. Reductive methylation studies of the Lys 394 region. *Biophys. J.* **64**, 792-802

10.   McGovern, R. E., Snarr, B. D., Lyons, J. A., McFarlane, J., Whiting, A. L., Paci, I., Hof, F., and Crowley, P. B. (2015) Structural study of a small molecule receptor bound to dimethyllysine in lysozyme. *Chem. Sci.* **6**, 442-449

11.   Abraham, S. J., Hoheisel, S., and Gaponenko, V. (2008) Detection of protein–ligand interactions by NMR using reductive methylation of lysine residues. *J. Biomol. NMR* **42**, 143-148

12.   Hattori, Y., Furuita, K., Ohki, I., Ikegami, T., Fukada, H., Shirakawa, M., Fujiwara, T., and Kojima, C. (2013) Utilization of lysine (1)(3)C-methylation NMR for protein-protein interaction studies. *J. Biomol. NMR* **55**, 19-31

13. Volkov, A. N., Ubbink, M., and van Nuland, N. A. J. (2010) Mapping the encounter state of a transient protein complex by PRE NMR spectroscopy. *J. Biomol. NMR* **48**, 225-236

14. Wien, R. W., Morrisett, J. D., and McConnell, H. M. (1972) Spin-label-induced nuclear relaxation. Distances between bound saccharides, histidine-15, and tryptophan-123 on lysozyme in solution. *Biochemistry* **11**, 3707-3716

15. Iwahara, J., Schwieters, C. D., and Clore, G. M. (2004) Ensemble Approach for NMR Structure Refinement against 1H Paramagnetic Relaxation Enhancement Data Arising from a Flexible Paramagnetic Group Attached to a Macromolecule. *J. Am. Chem. Soc.* **126**, 5879-5896

16. Delaglio, F., Grzesiek, S., Vuister, G. W., Zhu, G., Pfeifer, J., and Bax, A. (1995) NMRPipe: A multidimensional spectral processing system based on UNIX pipes. *J. Biomol. NMR* **6**, 277-293

17. Johnson, B. A., and Blevins, R. A. (1994) NMR View: A computer program for the visualization and analysis of NMR data. *J. Biomol. NMR* **4**, 603-614

CHAPTER 4: DEVELOPING AN AFM TECHNIQUE TO OBSERVE PROTEIN-PROTEIN COMPLEXES

4.1. Studying Protein Complexes using AFM

The attachment of proteins to surfaces for atomic force microscopy (AFM) study is a critical field for the development of bioelectronics or biosensor devices, due to its application of target protein interaction with selective surfaces. Several studies have been published with established methods for binding proteins to surfaces using particle lithography (1-5). The creation of a disulfide bond between a cysteine on the target protein and a free thiol on the substrate surface is one such method. When the protein has only one cysteine residue, the protein is anchored in a particular orientation. Further studies of protein-protein complexation can be performed to confirm the location (or steric hindrance) of a binding site on the protein.

The purpose of this work is to develop a versatile method for the study of protein-protein interactions using AFM. The model interaction chosen is the complex formed between the cysteine protease, papain, and a cysteine protease inhibitor (ICP). The ICP-papain interaction is both tight-binding and binds in a ratio of 1:1, making the complex an ideal candidate for method development. Successful study of this complex will pave the way for future studies of surface imaging for other protein-protein interactions. In this study, we report the successful anchoring of a mutant of ICP from *Leishmania mexicana* to a modified surface using a simple disulfide bond formation between the single cysteine of the protein and the free thiol head-group of the surface. Images acquired with AFM confirm the collection of the protein as a single monolayer inside the 3-mercaptopropyl-trimethoxysilane (MPTMS) pores. The approximate height of the protein was measured by imaging ICP bound to an ultra-flat mica thin film and found to be comparable to the observed change in height within the pores. The protein-modified surfaces

were then washed with papain to determine whether or not the exposed end of ICP contained the binding site.

4.2. Materials

Single-side polished Si(111) doped with boron (Ted Pella, Inc.) was used as the substrate for AFM studies. Papain isolated from papaya (*Carica papaya*), sulfuric acid (95%), hydrogen peroxide (30%), anhydrous toluene, sodium chloride (NaCl), sodium phosphate dibasic, sodium phosphate monobasic, dithiolthreitol (DTT), imidazole, tris(hydroxymethyl)aminomethane (tris), and Tween 20 were purchased from Sigma-Aldrich. 2-[Methoxy(polyethyleneoxy)propyl]-trichlorosilane (PEG-silane) and 3-mercaptopropyl-trimethoxysilane (MPTMS) were purchased from Gelest. Luria broth (LB) and agar were purchased from BD Biosciences. Tris(2-carboxyethyl)phosphine hydrochloride (TCEP), immobilized TCEP, Coomassie Plus protein assay, and bovine serum albumin protein standard were purchased from Pierce. Other chemicals and materials used include OverExpress C41(DE3) cells (Lucigen), isopropyl β-D-1-thiogalactopyranoside (IPTG, Affymetrix Anatrace), complete EDTA-free protease inhibitor (Roche Life Science), 10x BugBuster protein extraction reagent (EMD Millipore/Novagen), Ni Sepharose 6 FastFlow (GE Healthcare), 2,2'-dipyridyldisulfide (Alfa Aesar), disulfide derivatized 2D carboxymethyldextran chip (Xantec), 500 nm silica mesoparticles in suspension (Fisher Scientific), monodisperse silica powder (Fiber Optic Center, Inc.), and ACS grade ethanol (Pharmco-Aaper). All water used was supplied from a Millipore Direct-Q 3 ultrapure water system.

4.3. Expression and Purification of *L. mexicana* ICP mutant.

A pET28 plasmid encoding *L. mexicana* ICP with an N-terminal 6XHis-tag was supplied by from Brian O. Smith, University of Glasgow, Glasgow, UK (6). The plasmid encodes for a

double mutant to produce a protein with a single cysteine residue: C56S, V46C. C41(DE3) *E. coli* cells were transformed with the plasmid and grown in 1 L of LB media with 50 µg/mL kanamycin at 37 °C until an optical density at 600 nm of 0.6-0.8 was reached. The culture was induced with 1 mL of 1 M IPTG and grown at 17 °C for 20 h. The cells were harvested and lysed using BugBuster in lysis buffer (10 mM Tris, 150 mM NaCl, 10 mM imidizole, pH 7.5) and sonicated on ice (3 iterations of a 30/10 seconds on/off pulse cycle at 40% power). Cleared lysate was obtained by centrifugation at 30,000 g for 30 min at 4 °C, and the protein was purified by Ni-affinity chromatography. A 2 mL column bed of Ni Sepharose Fast Flow was equilibrated with 4 mL of 20 mM sodium phosphate, 500 mM sodium chloride, 50 mM imidazole at pH 7.4. The cleared lysate was loaded onto the column and washed with 5 mL of the same equilibration buffer. The protein was eluted with 2 mL of 20 mM sodium phosphate, 500 mM sodium chloride, 500 mM imidazole at pH 7.4, and further purified by gel filtration chromatography using a Hiprep 26/60 Sephacryl S-100 column (GE Healthcare) and 20 mM potassium phosphate, 150 mM NaCl buffer at pH 7.2. The protein elution was collected and analyzed using SDS-PAGE to confirm the purity and identity of the protein.

4.4. Creation of Nanopatterned Surfaces.

Surfaces of nanopatterned MPTMS pores within a matrix of PEG-silane on Si(111) were prepared using the particle lithography procedure previously reported by Englade-Franklin *et al.* in section 2.2 of their work (7). Figure 4.1 is a graphical overview of this procedure. Silicon substrates were rinsed with deionized water, dried with argon, and submerged in a 3:1 (v/v) solution of sulfuric acid and hydrogen peroxide for cleaning. After 90 min, the substrates were removed from the cleaning solution, rinsed with deionized water, and dried under argon. The substrates were placed on a raised platform in a reaction vessel over a deposit of 400 mL of

MPTMS. The vessel was heated in an oven at 70 °C for 4 hours to generate a vapor of MPTMS to produce a thin film of MPTMS over the surface of the substrates. The substrates were then washed with ethanol, rinsed by sonication in ethanol for 30 min, and then dried under a stream of argon.

A suspension of silica mesoparticles (0.1g in 10 mL ethanol) was cleaned by washing four times using centrifugation and resuspension in deionized water. A surface mask was prepared by depositing 10 μL of the silica mesoparticle suspension onto each MPTMS/Si substrate and dried at 4 °C for 16 hours. The substrates were then treated with UV–ozone for 20 min to oxidize exposed areas between the particle masks to form silanol functional groups. Immediately, the samples were immersed in a 1% (v/v) solution of PEG-silane in anhydrous toluene for 5 hours. Areas that were exposed to UV–ozone refilled with PEG-silane, while areas underneath the silica mesospheres remained protected. The reaction was quenched with deionized water, and the silica mesopheres were removed by sonication in ethanol for 30 mins. The final nanopatterned substrates were dried under argon.
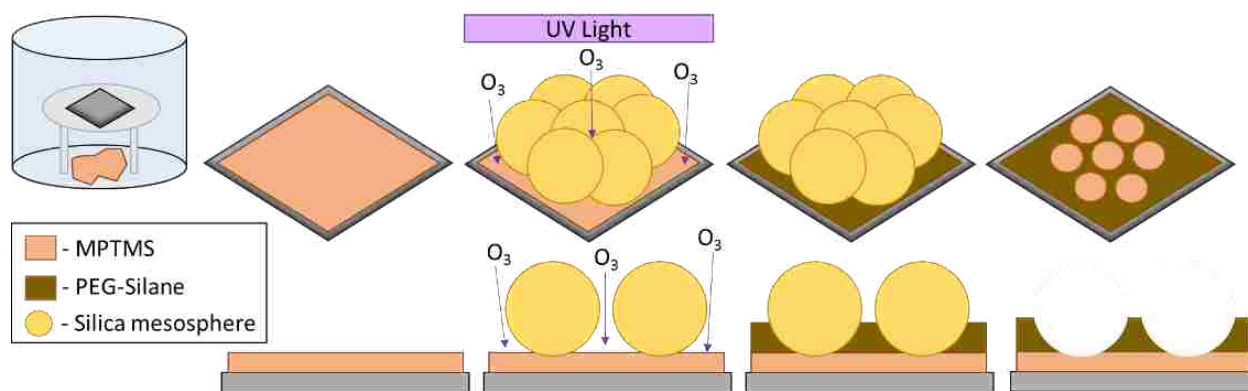

Figure 4.1: Particle lithography procedure for the creation of MPTMS nanopores in PEG-silane on a silicon(111) substrate.

4.5. Attachment of ICP to Nanopatterned Substrates for AFM.

To reduce the exposed thiols on the substrate surface and prepare them for disulfide bonding with the protein, the nanopatterned substrates were submerged in a solution of 10 mM TCEP at room temp for 5 h and then rinsed with deionized water. ICP is prone to forming disulfide bonds in solution, therefore the ICP mutant was reduced using immobilized TCEP. A bed of 1 mL of immobilized TCEP resin was incubated with 250 µg of ICP in gel filtration buffer for 1 hr and eluted using the same buffer. An aliquot of the elution was concentrated to 90 µg/mL as determined by the Coomassie Plus Protein assay (Pierce) using a bovine serum albumin standard. The substrates were submerged in 2 mL of 90 µg/mL reduced ICP at 4°C for 16 h. The substrates were rinsed successively with 20 mM sodium phosphate, 150 mM sodium chloride buffer at pH 7.5, followed by deionized water, twice each, to remove non-specifically bound protein. The substrates were dried under a stream of argon and then analyzed with tapping-mode AFM. To confirm ICP binding through a disulfide bond, the substrates were rinsed successively with 20 mM TCEP followed by deionized water. A figure of the ICP-bound substrate before and after rinsing with TCEP can be found in Appendix A3.

4.6. Height Confirmation of ICP with Mica Thin Film

To confirm that the height recorded in filled MPTMS pores was due to the anchoring of ICP, protein was attached to a flat, ultra-thin film of mica. A 1:100 dilution was made of the 90 µg/mL sample of ICP and 15 µL of this dilution were deposited onto a freshly separated sheet of mica. The film was allowed to dry at room temperature for 2 hours and then immediately imaged and characterized using tapping-mode AFM.

4.7. Study of Papain-ICP Interaction with AFM.

The ICP-modified substrates were submerged in a solution of 50 µg/mL papain in water for 16 h at 4 °C. The samples were rinsed successively with 20 mM sodium phosphate, 150 mM

sodium chloride buffer to remove non-specifically bound protein. A final rinse was done with deionized water. The samples were dried under a stream of argon and then characterized using tapping-mode AFM.

4.8. Instrumentation

Scanning probe studies were performed using a 5500 instrument with PicoView (v. 1.12) software (Agilent Technologies, Tempe, AZ). Probes were acquired from Applied Nanostructures (ACTA, resonant frequency 300 kHz, k = 37 N m^{-1}). Images were taken in tapping mode, and then processed and analyzed using Gwyddion (v. 2.15), which is free software supported by the Czech Meteorology Institute (8).

4.9. Results

AFM images of substrates modified with MPTMS and PEG-silane show uniformly patterned nanopores that are approximately 5.5 nm deep. The images derived from phase shift of the cantilever versus distance show a clear difference between the nanopores and the rest of the surface, indicating that the chemical composition of the surface within the nanopores is different from that of the surrounding area. Cursor profiles confirm the presence of pores and allow for height determination (Figure 4.2a-c).

After submerging the substrate in the reduced ICP V46C solution, the topography images showed a visible collection of new heights within the nanopores, though they do not appear to be filled to capacity. Cursor profiles show that the height difference decreased across all pores. An example of this height change can be observed in the Figure 4.2d-f. Rinsing the substrate with TCEP to reduce the disulfide bonds returned the surface of the substrate to its unmodified form, and the height difference between the pores and the PEG-silane surface returned.

ICP on mica thin films provided height measurements for the protein. Multiple cursor profiles were taken to develop a histogram of maxima. The average height of 100 cursor profiles was determined to be 2.9 ± 0.6 nm. An example of a sampling of cursor profiles is in Figure 4.3. A full set of images used for the histogram of protein heights is in Appendix A3.
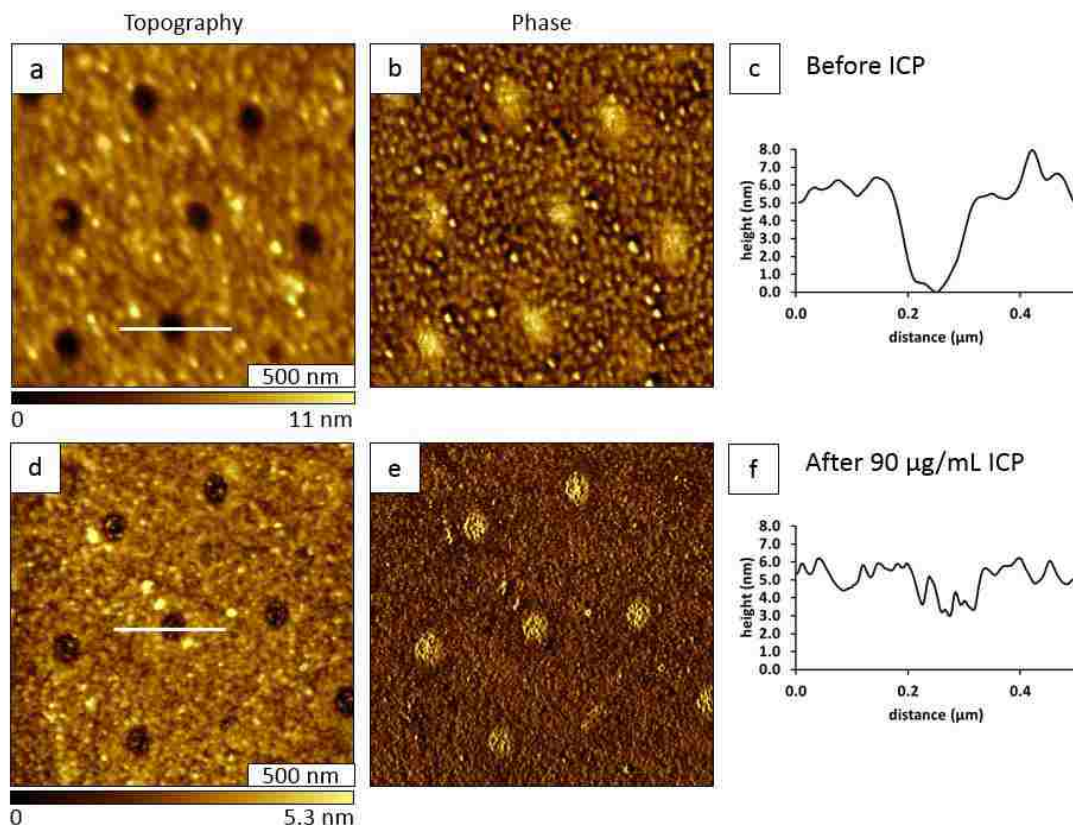
Figure 4.2: MPTMS pores in PEG-silane before (a-c) and after (d-f) the addition of ICP V46C. Topography images (a and d) show the appearance of raised spots within the pores after protein addition. Phase images (b and e) highlight the difference in chemical composition along the surface. Cursor profiles (c and f) are derived from the white line as seen in topography images a and d.
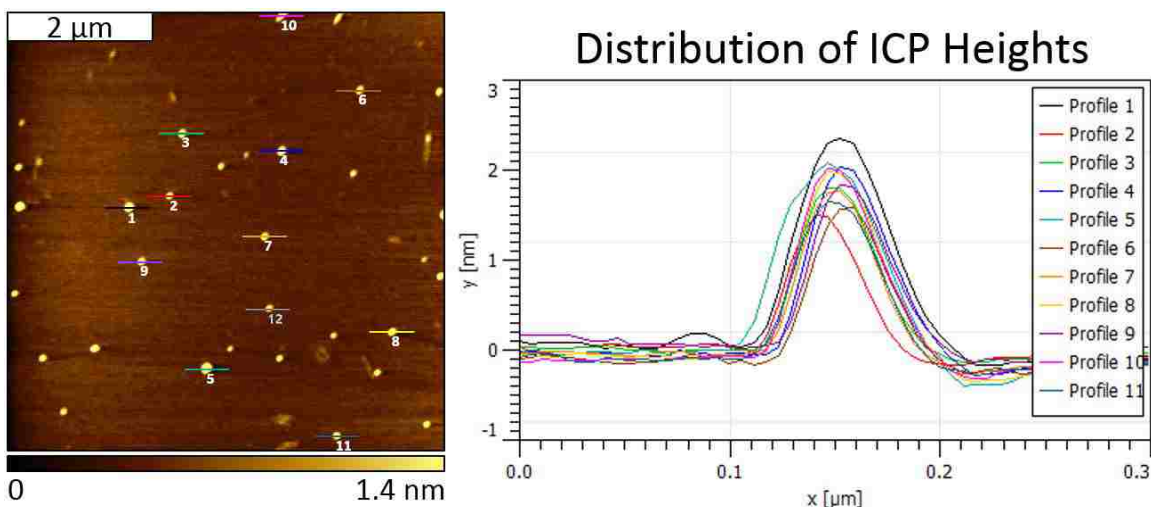
Figure 4.3: A topography image of ICP on an ultra-thin film of mica used for the determination of the height of the protein. Cursor profiles are derived from lines over the center of raised areas in the topography image. This figure is one of several images taken to determine the distribution of heights. The other images can be found in the appendix.

The histogram can be seen in Figure 4.4. For comparison, Chimera software developed by UCSF (9) was used to obtain the protein's dimensions based on the 3-dimensional NMR structure (PDB ID #2C34). Since proteins are dynamic and constantly in motion, a single set of defined dimensions is not feasible. This model can be seen in Figure 4.5.
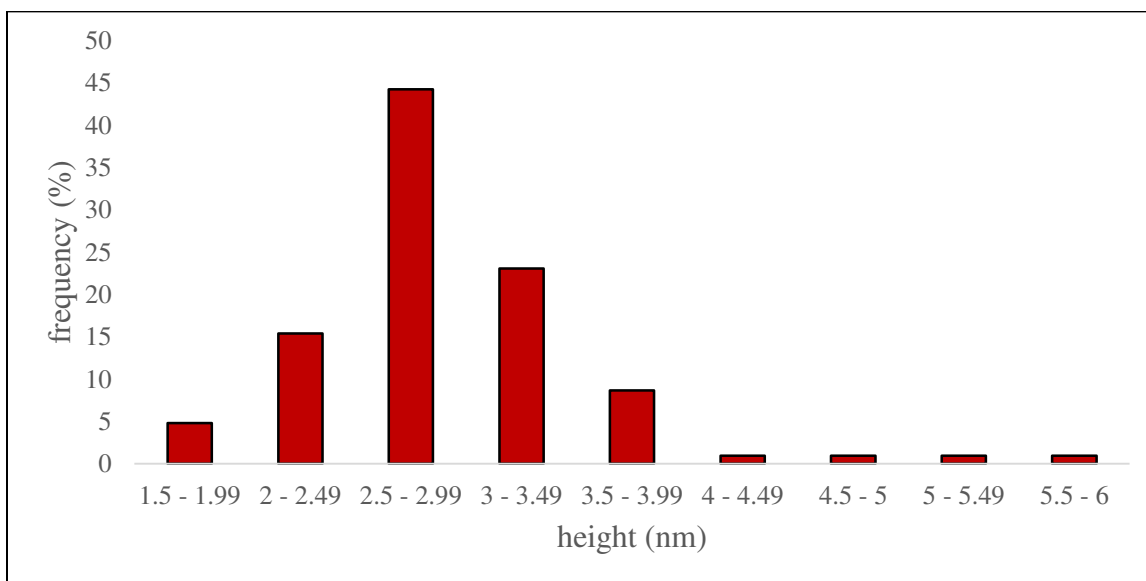
Figure 4.4: A histogram of heights taken from 100 cursor profiles of raised areas of ICP on an ultra-thin film of mica. The average height was determined to be 2.9 ± 0.6 nm.
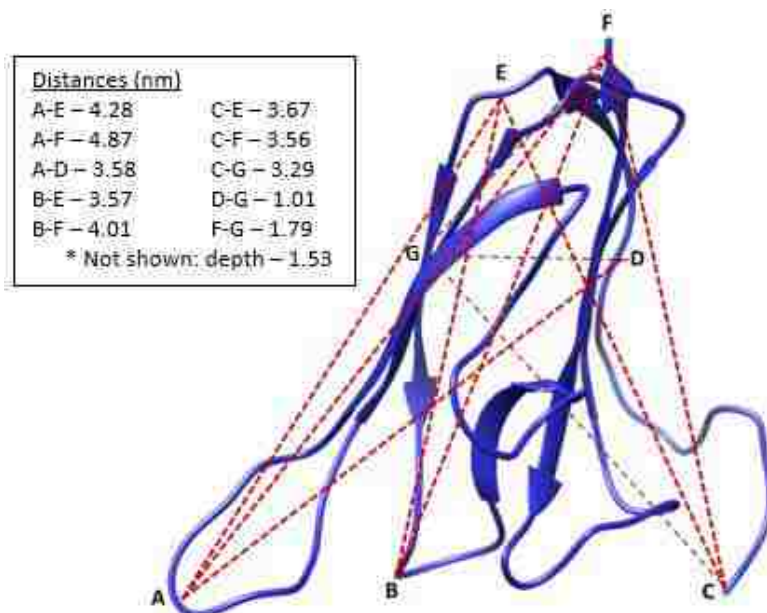
Figure 4.5: A model of ICP (6) with various distance measurements taken across the protein, to establish a rough model of expected protein dimensions.

Another possibility for comparison of dimensional data comes from the average diameter of ICP as calculated using the CalcTool online calculator (10). Based on 133 amino acids in the ICP sequence, the average diameter is determined by the tool to be 3.5 nm. However, the CalcTool does not take into account the ellipsoidal shape of the protein.

Submerging the substrate with anchored ICP in a solution of papain did not result in any change in height when analyzed with AFM. Many variations of the reaction conditions were tried, including varying degrees of protein concentration (anywhere from $20 - 200$ µg/mL), decreased salt concentration for the buffer, and increased reaction time. No modifications resulted in any positive results. Papain did not selectively bind to the ICP anchored within the pores.

4.10. Discussion

The uniform filling of MPTMS pores on the substrate surface indicates successful disulfide bonding between the exposed thiol in the pore and the free cysteine residue of the ICP mutant. The disulfide bond was confirmed when the substrate was rinsed with a TCEP solution

meant to reduce disulfide bonds – cursor profiles showed the return of pores, and the height gain from the protein disappeared. The addition of the protein to the MPTMS pores caused the height profile to increase approximately 3.0 nm. This is expected to be a monomer layer of the protein within the pore. The average height determined for ICP on the ultra-thin films of mica was 2.9 ± 0.6 nm, which agrees with the data collected from cursor profiles of ICP in MPTMS pores. These values also agree with the range of distances measured from the protein model in Chimera. It should be noted that a direct comparison is difficult to make because the protein is dry in the AFM measurement and hydrated in the structure. It is likely that when sufficiently dried, as in the AFM studies performed in this work, ICP collapses into a smaller size due to denaturation. Denaturation would also explain why papain was unable to bind to immobilized ICP within the pores.

4.11. Future Work

The ICP-papain complex remains an excellent model for method development of protein interaction studies. Future work should be done to perfect observation of this model using AFM techniques, such as taking advantage of liquid imaging techniques as opposed to allowing the protein to dry on the substrate surface. The potential is great for this method of protein-protein interaction study using AFM to become universally applicable, and it will be a critical stepping stone for the observation of other protein-protein interactions with AFM.

The inability to observe papain binding with ICP has been a hindrance. Steps need to be taken to allow for the protein-protein interaction to occur. As the binding of ICP and papain in solution proceeds as would be expected, it can be assumed that the problem lies with the involvement of the AFM chip surface, or that ICP is denatured on the surface, rendering it incapable of binding to papain. Another possibility is that ICP's orientation on the surface is

unfavorable. Other mutants of ICP could be anchored to the chip, as this would cause different areas of the protein to be available for binding. It is possible that anchoring at the 46 position (V46C) does not allow for enough exposure of the ICP's binding site.

The differences between the expected dimensions of ICP taken from the model and the measured heights of ICP observed on the ultra-thin mica film may only be a mild discrepancy, but steps can be taken in the future to correct for this difference. With the use of AFM imaging techniques in liquid systems, liquid imaging of substrates would give a more accurate representation to the behavior of proteins in native conditions. Many techniques exist that use liquid imaging to observe protein samples with AFM. The adaptation of one of these established techniques would likely give results that are more indicative of the behavior of our proteins in native conditions.

4.12. Conclusion

The ICP V46C mutant of ICP was successfully anchored to a modified AFM surface through disulfide bond formation between the single cysteine of the protein and the free thiol head-group within the surface pore. Images acquired with AFM confirm the collection of the protein inside the MPTMS pores, and cursor profiles across the pores display the height change associated with anchoring selectively within the pores. The approximate height of the protein was confirmed by imaging of ICP bound to an ultra-flat mica thin film. This confirmed height was slightly shorter than the height expected for ICP based on distance calculations with computer models. This difference is believed to be due to the nature of the protein in solution versus dehydrated on a surface.

Washing the protein-modified surfaces with papain produced no change in height and no usable images, which is believed to be due to denatured ICP in dry conditions or due to steric

hindrance of the binding site based on the orientation of ICP anchored in the MPTMS pores. Future work will hopefully eliminate this problem with the perfection of reaction conditions involving papain, the development of an in-liquid imaging technique compatible with this protein-protein interaction, and potentially the use of a different ICP mutant. Forcing the orientation of ICP within the MPTMS pore to change may give better exposure of ICP's binding site and allow for the complexation with papain.

4.13. References

1.   Cai, Y., and Ocko, B. M. (2005) Large-Scale Fabrication of Protein Nanoarrays Based on Nanosphere Lithography. *Langmuir* **21**, 9274-9279

2.   Garno, J. C., Amro, N. A., Wadu-Mesthrige, K., and Liu, G.-Y. (2002) Production of Periodic Arrays of Protein Nanostructures Using Particle Lithography. *Langmuir* **18**, 8186-8192

3.   Ngunjiri, J. N., Daniels, S. L., Li, J.-R., Serem, W. K., and Garno, J. C. (2008) Controlling the surface coverage and arrangement of proteins using particle lithography. *Nanomedicine* **3**, 529-541

4.   Taylor, Z. R., Keay, J. C., Sanchez, E. S., Johnson, M. B., and Schmidtke, D. W. (2012) Independently Controlling Protein Dot Size and Spacing in Particle Lithography. *Langmuir* **28**, 9656-9663

5.   Taylor, Z. R., Patel, K., Spain, T. G., Keay, J. C., Jernigen, J. D., Sanchez, E. S., Grady, B. P., Johnson, M. B., and Schmidtke, D. W. (2009) Fabrication of Protein Dot Arrays via Particle Lithography. *Langmuir* **25**, 10932-10938

6.   Smith, B. O., Picken, N. C., Westrop, G. D., Bromek, K., Mottram, J. C., and Coombs, G. H. (2006) The structure of *Leishmania mexicana* ICP provides evidence for convergent evolution of cysteine peptidase inhibitors. *J. Biol. Chem.* **281**, 5821-5828

7.   Englade-Franklin, L. E., Saner, C. K., and Garno, J. C. (2013) Spatially selective surface platforms for binding fibrinogen prepared by particle lithography with organosilanes. *Interface Focus* **3**, 20120102

8.   Nečas, D., and Klapetek, P. (2012) Gwyddion: an open-source software for SPM data analysis. *Cent. Eur. J. Phys.* **10**, 181-188

9.   Pettersen, E. F., Goddard, T. D., Huang, C. C., Couch, G. S., Greenblatt, D. M., Meng, E. C., and Ferrin, T. E. (2004) UCSF Chimera—A visualization system for exploratory research and analysis. *J. Comput. Chem.* **25**, 1605-1612

10.   Shipway, S., Shipway, A. (2008) CalcTool: Quick and easy everyday calculators.

5.1. Introduction

Actin is a protein that is found in all eukaryotic cells. It is highly conserved, with no more than 20% amino acid sequence difference between species. (1) Actin is 42 kDa in size and has a globular shape. Monomer units of actin polymerize into filamentous actin (F-actin) in the presence of adenosine triphosphate (ATP), facilitated *in vitro* by a divalent cation (Ca^{2+} or Mg^{2+}) and dithiothreitol. F-actin participates in many important cellular processes, such as cell motility, cargo transport, muscle contraction, and the formation of microfilaments to aid in structure and support of cells and muscle tissue. (1)

Proteins that interact with actin are called actin-binding proteins (ABPs). Due to variations in the definition of ABPs, there are between 60 and 100 known ABPs, which perform various functions and bind either globular actin or F-actin. (2) ABPs can be categorized into classes based on function: regulators of F-actin assembly and disassembly, regulators of higher-order F-actin structures, and proteins that use F-actin as a mechanical framework. (3) Many ABPs bind actin through two calponin homology domains, each approximately 100 residues with a conserved amino acid sequence. (4,5)

Binding studies of F-actin and ABPs are typically performed using ultracentrifugation and polyacrylamide gel electrophoresis (PAGE) or affinity chromatography. (6) F-actin and the ABP are centrifuged at high speeds to pellet F-actin and any ABP bound to it. The supernatant and pellet are analyzed with PAGE, and the relative concentrations in the supernatant and pellet are determined densitometrically. Binding is confirmed when the concentration of ABP in the

supernatant is lower than the concentration in the pellet. Affinity chromatography is another method that can be used to identify ABPs. Columns with F-actin immobilized on the stationary phase were invented in 1989 by Miller *et al.* (7) ABPs from complex mixtures, such as cell extracts, are selectively retained and separated from other proteins. Results from these methods are useful to identify ABPs and may indicate a role of the ABP in polymerization or depolymerization of F-actin, but to understand the binding mechanism, more sophisticated methods, such as microscopy, are needed.

Microscopy is used to image and analyze objects at the nm - µm scale. Biological samples can be studied with microscopy at the cellular and subcellular levels, including imaging individual organelles and protein networks like F-actin. Recent advances in the areas of fluorescence microscopy, atomic force microscopy, and cryo-electron microscopy have greatly improved our ability to study processes such as cell motility, filament assembly, and protein-protein interactions. The application of these methods to the study of actin filaments and ABPs has led to important discoveries concerning the behavior of F-actin in biological systems. This review describes the basics of these techniques and highlights recent microscopy studies that visualize F-actin and its interaction with various ABPs.

5.2. Fluorescence Microscopy

In fluorescence microscopy, the fluorescence emission from a sample is imaged. If a sample does not autofluoresce, then the sample is prepared for microscopy by labelling with a fluorescent marker or stain. A common method to study proteins, like actin and ABPs, is to express a recombinant fluorescent-fusion protein. Another option is to use fluorescent dyes, such as x-rhodamine, which specifically bind to the analyte. There have been two derivatives of

fluorescence microscopy used to study the binding dynamics of actin and ABPs: fluorescent speckle microscopy and total internal reflection fluorescence microscopy.

5.2.1 Fluorescent Speckle Microscopy

Developed in the 1990s by Waterman-Storer *et al.*, (8) fluorescent speckle microscopy (FSM) was originally used to investigate macromolecular assembly dynamics both *in vivo* and *in vitro*. (9) It is a derivative of fluorescent analog cytochemistry, in which fluorophore-labeled proteins are expressed or microinjected *in vivo* and are incorporated into macromolecular structures. (10-12) F-actin filaments were imaged using FSM by injecting x-rodamine-lableled actin into cells (Figure 5.1 (13)). As the labeled actin was incorporated into the filaments, the filaments appeared "speckled" due to the distribution of fluorescently labeled actin among unmodified-actin. (8)
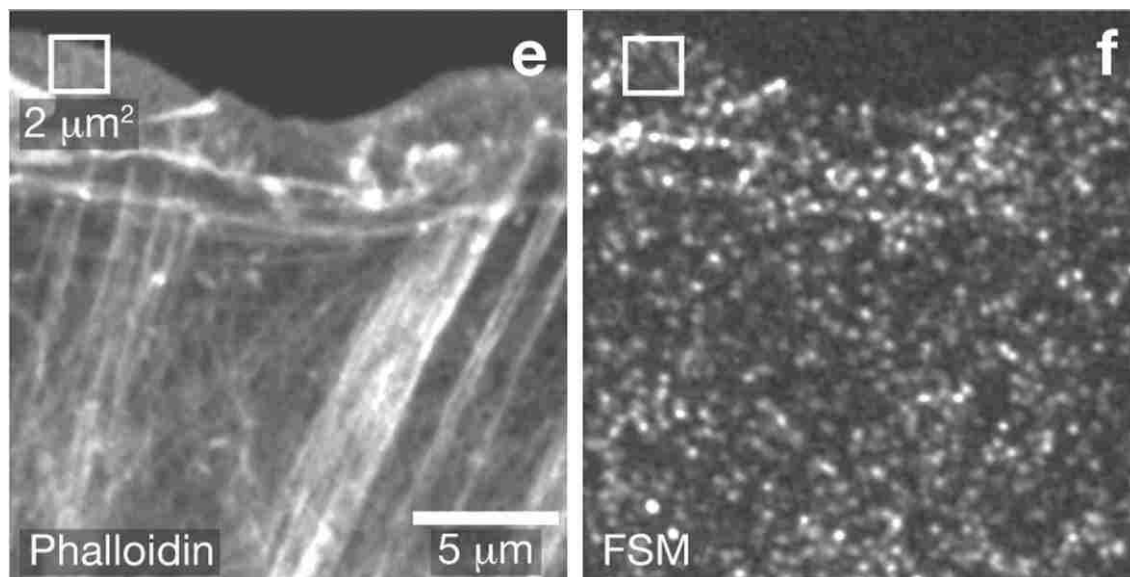
Figure 5.1: (13) Speckle formation of x-rhodamine-labeled actin filaments injected into an epithelial cell, fixed and then stained with Alexa-488 phalloidin. (e) The organization of F-actin in amorphous networks and bundles can be seen. (f) A single FSM image of actin filaments. Structural information appears to be lost, but time-lapse FSM series rectifies this loss and provides further motility and structure information.

Speckles can be visualized only if the ratio between labeled and endogenous molecules is low because a lower concentration results in the appropriate contrast between neighboring

diffraction-limited image regions. This contrast is only achieved via microinjection of the protein or a low level of expression. Speckle contrast can therefore be increased by decreasing the fraction of labeled molecules, but only to a point. Noise obscures speckle signals at very low concentrations. It has been found that optimal conditions for speckle fluorescence occur when the ratio of fluorophore-labeled molecules is between 0.5% and 2.0%. (9)

The behavior, turnover, and movement of biopolymers in filamentous forms, such as actin, can be observed using speckle fluorescence time-lapse microscopy. More recently, the use of FSM has been expanded from a single spectral channel to multispectral FSM. (14) This advancement has led to an emergence of studies in focal adhesion proteins, such ABPs, and their interactions with filamentous biomolecules, such as F-actin. (13)

5.2.2. Advantages of FSM

The low fraction of fluorescent subunits strongly reduces background fluorescence that may arise from unincorporated fluorescent molecules or those that may be out of focus. The distribution of speckles also allows for detection of movement and turnover of molecules when imaged over time. This dynamic process is impossible to see in the case of uniformly labeled filaments.

5.2.3. Study: Correlation of Actin Assembly with a GFP-p34 Signal

In biological systems, Arp2/3 is a protein complex that is thought to promote polymerization of networking filaments by aiding new filament creation from preexisting ones. This protein has been described in the literature as a mediator of actin, helping to regulate processes of polymerization and depolymerization in tandem. (15-17) It has been shown that Arp2/3 is present along the lamellipodium, the cytoskeletal protein actin at the mobile edge of cells. Interestingly, Arp2/3, detected with fluorescent stain, was also present in punctate patterns

within the lamella, a dense structure formed by the cell at the leading edge for cell motility and

migration. These observations led to speculation that Arp2/3 was clustering in areas of F-actin

assembly.
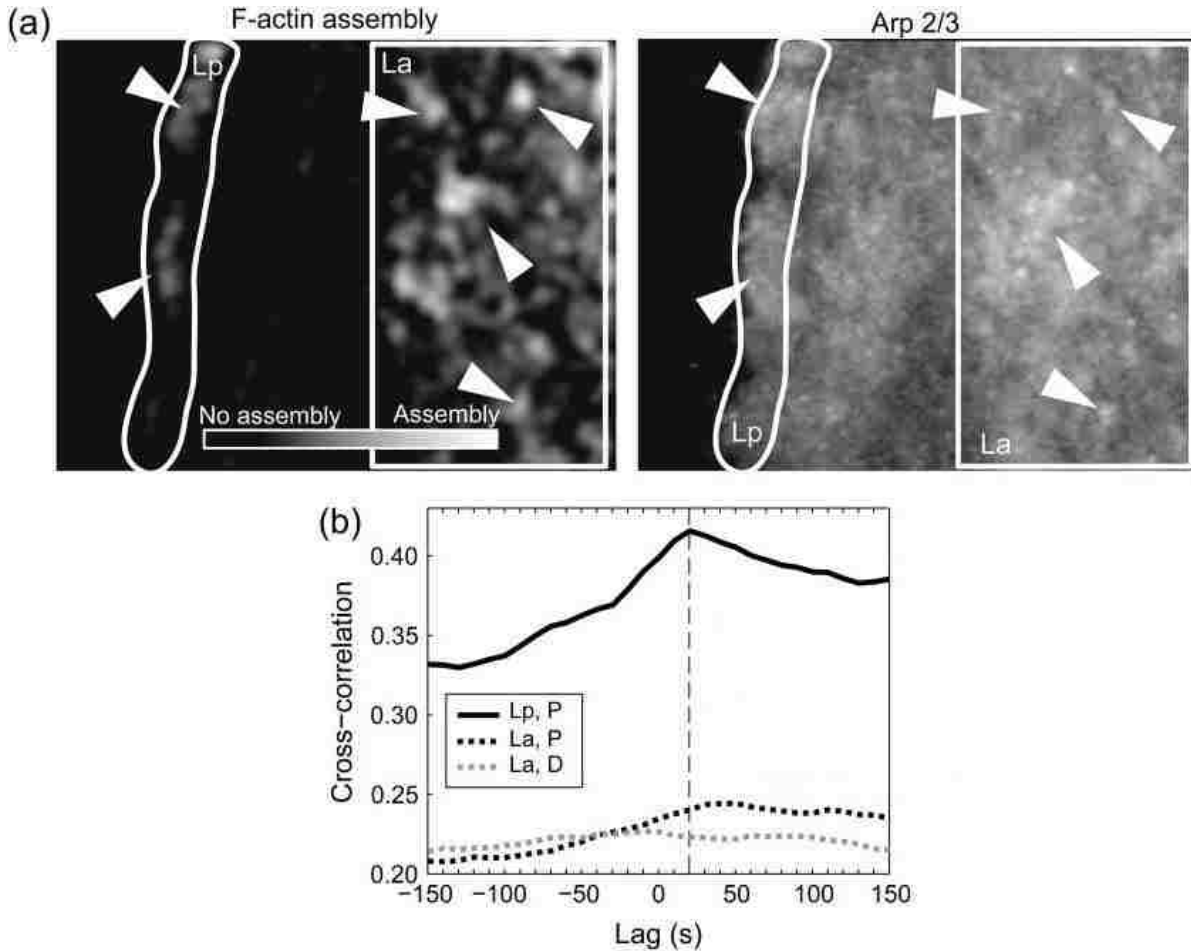
Figure 5.2: (18) Correlation between F-actin network assembly and the signal of GFP-p34 component of the Arp2/3 complex. (a-i) F-actin assembly, as measured by qFSM. Arrows indicate locations of higher assembly. (a-ii) Arp2/3 distribution, as shown by GFP-p34 signal. Arrows indicate higher populations of Arp2/3, which coincide with areas of higher F-actin network assembly. (b) Cross-correlations between GFP-p34 signal and F-actin assembly in the lamellipodium (solid line) and in the lamella (dark dashed line), and finally the cross-correlation between GFP-p34 signal and F-actin disassembly in the lamella (light dashed line).

Time-resolved quantitative FSM (qFSM) F-actin assembly and disassembly maps were

correlated with time-lapse images of the green fluorescent protein (GFP)-p34 component of the

Arp2/3 complex. (17) Figure 5.2 shows the correlation found between F-actin network assembly,

measured with qFSM, and the signal from the GFP-p34 component of the Arp2/3 complex. Pockets of higher F-actin network assembly, as seen by the bright spots in figure 5.2a-i, appeared to coincide with bright pockets of GFP-p34 signal as seen in 2a-ii; however, cross-correlation of the two maps over time produced an average correlation coefficient of 0.22, as shown in figure 5.2b (dark dashed line). The same, low correlation was observed between GFP-p34 and the disassembly map (shown in the supplemental material within (17)) of the F-actin network (light dashed line), indicating a correlation in space but not in time between F-actin assembly/disassembly and Arp2/3 complex.

These data illustrate the importance of nonsteady-state measurements and time-lapse qFSM. The processes of network assembly and disassembly and the accumulation of Arp2/3 in certain "hotspot" areas are both important observations that suggest a role for Arp2/3 in network organization. However, with dynamic analysis using time-lapse qFSM, the network processes and Arp2/3 accumulation were found to be independent of each other in time. Additionally, the correlation of qFSM data with image cues, such as accumulation or sudden lack of fluorescent signal or the apparent relocation of speckles, allows for the examination of functional relationships between proteins.

5.2.4. Total Internal Reflection Fluorescence Microscopy

Studying processes on surfaces with fluorescence microscopy can be a challenge with conventional techniques because of noise from fluorophores that have bound to the surface or are present in the surrounding medium. To circumvent this problem, Daniel Axelrod combined total internal reflection with microscopy as a tool to study surfaces and called the new method total internal reflection fluorescence microscopy (TIRFM). (19) In TIRFM, an evanescent wave is generated from light that, at a given incident angle, is internally reflected along the glass-sample

interface. It is a technique for studying occurrences at surfaces, such as cell surfaces and membranes, because the evanescent wave only penetrates to a depth of approximately 100 nm into the sample. This thin layer is called the "evanescent field," and it exponentially decays in intensity with increasing distance from the surface.

TIRFM has been in use longer than other microscopy methods, so F-actin and ABPs have been extensively studied using this method both *in vitro* and *in vivo*. Some recent studies of actin and ABPs with TIRFM include studies on the stabilization of actin, (20) the adhesion of actin to surfaces via ABPs, (21)the properties of ABPs, (22) and the visualization of actin assembly. (23)

5.2.5. Advantages of TIRFM

TIRFM allows for direct observations of biochemical and biological processes at the surface of a sample. Without perturbing the system, TIRFM allows for the study of protein functions involved in actin polymerization and related regulatory processes within the cell. It is also a method that does not require stabilization of the actin filaments, so observations can be made in native conditions.

5.2.6. Study: Assembly of F-actin Barbed Ends in Association with Formins

Formin proteins are a family of proteins known to act as actin assembly aids. Each contains a formin homology 2 (FH2) domain that promotes F-actin assembly by assisting and accelerating elongation at the barbed end of the filament. The FH2 domain is approximately 400 residues in length and, in all known cases, forms a dimer. (24)

TIRFM was used to observe the polymerization of F-actin in the presence of formin proteins. Glass slides were preincubated with NEM myosin-II, which bound to actin filaments and anchored them to the slide, leaving both the barbed end and the pointed end of the filaments free (figure 5.3a). The actin filaments were exposed to formins in solution to observe

polymerization. TIFRM images (figure 5.4) show that the barbed end of the filament elongates while the pointed end does not. This observation confirms that formin-aided F-actin polymerization occurs at the barbed end of the filament.
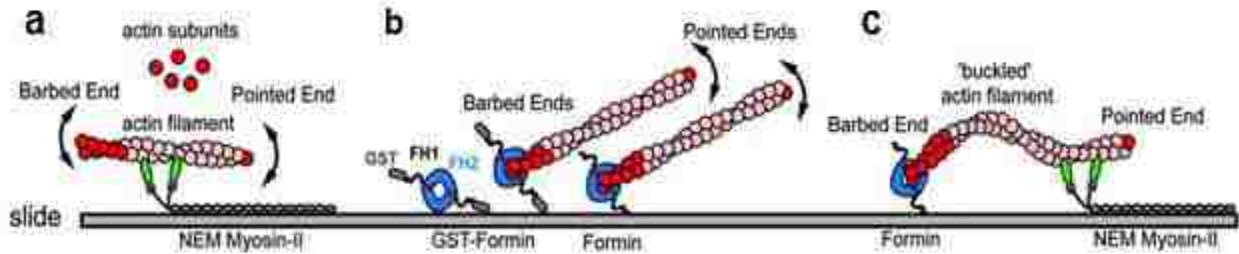
Figure 5.3: (22) A schematic of F-actin attachment on slides coated with NEM-myosin II (a), formin or GST-formin (b), and NEM-myosin II and formin (c).
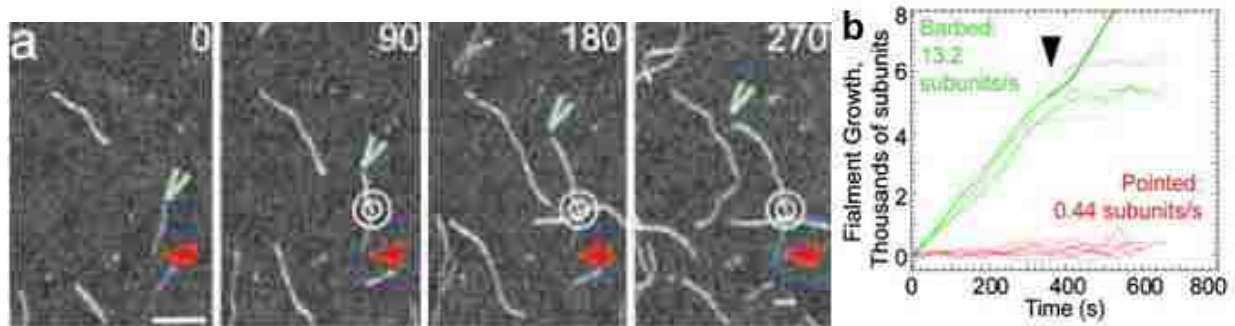
Figure 5.4: (22) The growth of F-actin bound to a glass slide by NEM myosin-II. White cirlces are the point of binding. Red arrows point to the pointed end of the filament. Green arrows point to the barbed end. Scale bar = 5 µm. The graph shows the length from the point of binding to each end of the filament.

In a second set-up, F-actin was exposed to glass slides preincubated with formins, and bound to the anchored formins by the barbed end of the filament (figure 5.3b). (22) Elongating filaments did not appear to dissociate from the immobilized formin, as seen in the TIFRM images (figure 5.5). Since polymerization occurs at the barbed end of the filament, it follows that insertional polymerization must be occurring. This conclusion was confirmed by the observation that filaments grow even when bound by NEM myosin-II and the barbed end was bound by formin (schematic in figure 5.3c).

F-actin was polymerized on slides preincubated with both a formin and NEM-myosin II, which provided a second attachment point for the filament (figure 5.3c). When tethered by NEM-myosin II, growth of the F-actin caused it to buckle, which appears in the TIRFM image as a loop between the two points of attachment. The force of polymerization that caused buckling was calculated in this study using a derivation of the Euler equation for maximum axial load on a column (27). Forces ranging from 0.25 – 1.3 pN were measured, with smaller filaments of actin producing higher forces.
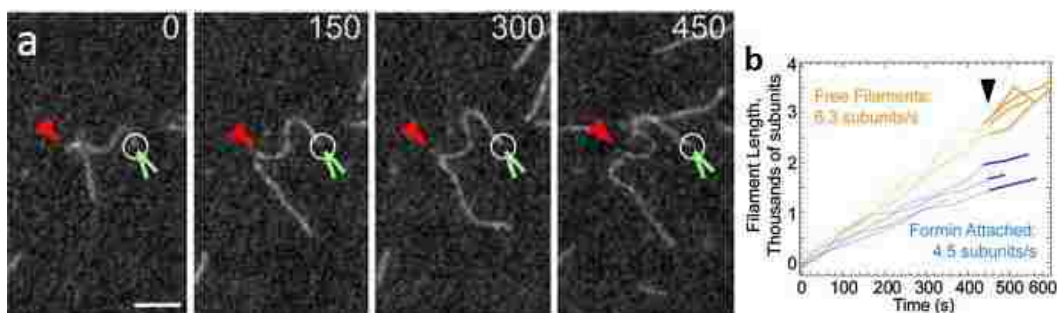
Figure 5.5: (22)The growth of F-actin on the slide at its barbed end is observed with TIRFM. White circles indicate the points at which filaments are attached at their barbed end to formin. The free filaments of actin grow linearly, while the filaments with the bound barbed end buckle in the middle during growth. Scale bar = 5 µm. The graph shows the length of the filaments as they increase over time.

5.2.7. Fluorescence – Conclusion

Fluorescence microscopy is a powerful and versatile tool for the study of actin filaments and APBs. The impact that an ABP can have on the structure, polymerization, motility, or stability of actin can be viewed in native conditions. Time-lapse FSM proves beneficial for the study of actin filament dynamics, providing visual evidence of movement and structural changes over time. TIRFM is useful for studies at surfaces and cell membranes, providing high-contrast and high-resolution images of biochemical processes that answer questions about the molecular nature of proteins and their interactions.

5.3. Atomic Force Microscopy

While the dynamic behavior of proteins can be studied using fluorescence microscopy, the resolution of the technique is limited to 0.5 µm. (28) Atomic force microscopy (AFM) is a molecular imaging method that can produce images of biological samples in aqueous solutions with lateral resolution of 1 nm and height resolution of less than 1 Å, (29-31) making it suitable for studying the structural properties of actin and ABPs. Sample imaging with AFM involves the acquisition of sample height information across many points of a sample surface. Resolution is limited by the number of data points and the speed is limited by the imaging rate.

High-speed AFM (HS-AFM) in tapping mode was developed by the Hansma and the Ando research groups to increase the imaging rate of AFM. (32,33) HS-AFM has been used to capture an image of a protein molecule within 100 ms without disturbing the structure or the function of the protein. (34) This technique makes ms − s dynamic measurements with AFM possible. Recent imaging studies with HS-AFM have captured images of F-actin remodeling (35) and time-lapse videos of actin/ABP interaction. (34)

5.3.1. Advantages of AFM

AFM can provide higher resolution images of proteins compared to fluorescence microscopy. The technique does not disturb the integrity or motility of the protein. There is no need for fluorescent markers or staining of the sample to be imaged by AFM. The molecules themselves are imaged, as opposed to imaging the fluorophores in fluorescence microscopy.

5.3.2. Study: AFM of F-Actin Remodeling when Bound by Drebrin A

High-resolution AFM was used by Sharma *et al.* to analyze the interaction between drebrin A, a major neuronal ABP, and F-actin. (35) Figure 5.6 shows AFM images of actin filaments alone (A, C) and with bound drebrin (B, D) over a mica substrate, at both low and high resolution. F-actin alone was shown to have a helical pitch of 36 ± 2 nm, consistent with

previous studies. (36) Drebrin binds to actin with regular periodicity along the filament, giving an image described as a "pearl necklace" like morphology. Height and periodicity variations across the F-actin backbone (both bound and unbound) can be seen in the graphs of Figure 5.6E and 5.6F. The peak periodicity profile of the F-actin filaments increases from 36 nm to 40 nm when bound to drebrin, demonstrating that the helical pitch of F-actin increases as a result of binding drebrin.
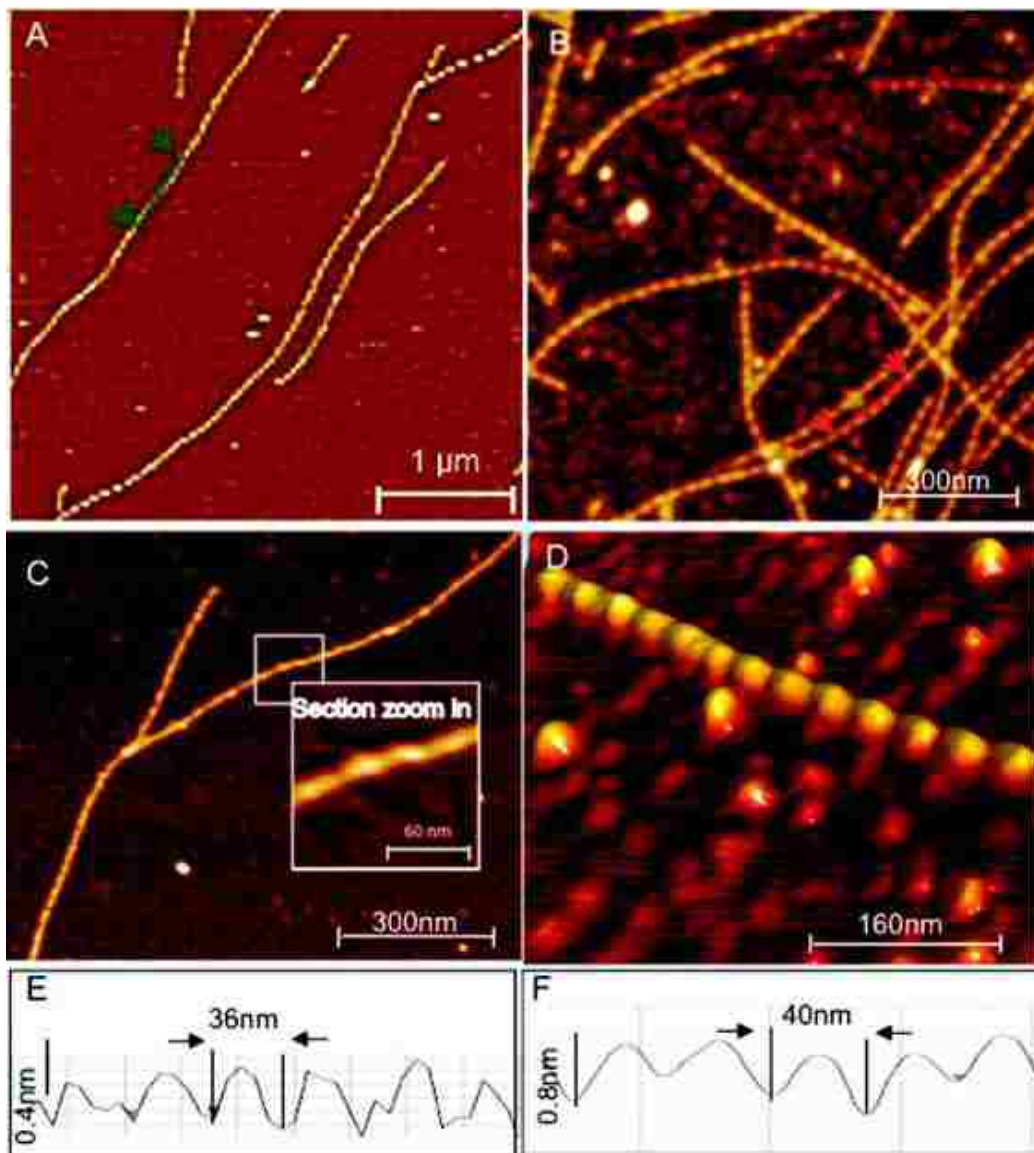

Figure 5.6. (37)Drebrin–F-actin complex. AFM images of unbound F-actin (A, C) and drebrin-bound F-actin (B, D) at lower (A, B) and higher (C, D) resolution. E and F display periodicity and height profiles obtained from arrowed areas in A and B.

AFM was also used to determine the helical pitch of F-actin bound with cofilin. Cofilin is a 16 kDa ABP that severs "overtwisted" F-actin by means of capturing and stabilizing. (38) Unlike drebrin, cofilin decreases the helical pitch of F-actin when bound. (38) AFM images of F-actin filaments bound with cofilin confirmed a significantly lower helical pitch (average 28.7 nm) (Table 1). While drebrin modifies F-actin by increasing the helical pitch and persistence length of filaments, cofilin has the opposite effect.
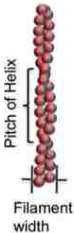
$n \sim 50$	F-actin	F-actin + drebrin	F-actin + cofilin
filament width (nm)	18.6 ± 2	40.5 ± 2.0	30.4 ± 2.6
pitch of helix (periodicity) (nm)	36 ± 2	40.0 ± 0.8	28.7 ± 2.1^b
persistence length Lp (AFM) (μm)	7.05^a	10.9	1.47^c
elastic modulus (Y) (MPa)	144	225	30.3

Table 1. [38] Comparison of ABP-bound F-actin Filaments. a: (39) and (40), b: (41), c: (42)

5.3.3. Study: Hand-Over-Hand Motion of Myosin V on F-actin

Double-headed myosin V (M5) homodimer is a member of the myosin superfamily of proteins. Its primary function in cells is cargo transportation. It has been shown to progressively move along an actin filament, 36 nm at a time, (43) as it binds and unbinds itself along the way. (44) This motion is described as "hand-over-hand", meaning that the two heads, the *N*-terminal domains, of the M5 homodimer alternately step ahead of each other as though it were "crawling" or "walking" forward. While this behavior has been accepted and implied in studies using single-molecule fluorescence microscopy, (45-47) it was not visualized until recently when the Ando group obtained high-resolution HS-AFM images of M5 "walking" across F-actin. (34,48)

To obtain the HS-AFM images of M5 "walking", actin filaments were immobilized on a surface through partial biotinylation of the actin followed by interaction with an electrically

neutral biotin-lipid bilayer surface formed on mica. Tail-truncated M5 (M5-HMM) was added in solution, and movement of M5-HMM homodimer was visualized at 7 frames per second (fps), as shown in figure 5.7a. Steps appeared to be approximately 36 nm in size, and unique structural features were observed. First, the area at the junction of the motor domain of the leading head appears to be smooth, while that at the trailing head has a V-shape (schematic in figure 5.7b). Second, the coiled tail of M5-HMM tilts towards the minus end of F-actin. Since these features occurred universally and reproducibly, they provide a marker of the polarity of the actin filament when bound M5-HMM is stationary. A third observation is that M5-HMM appears to bind at the groove between actin filaments, taking step sizes based on the pitch of the helix.

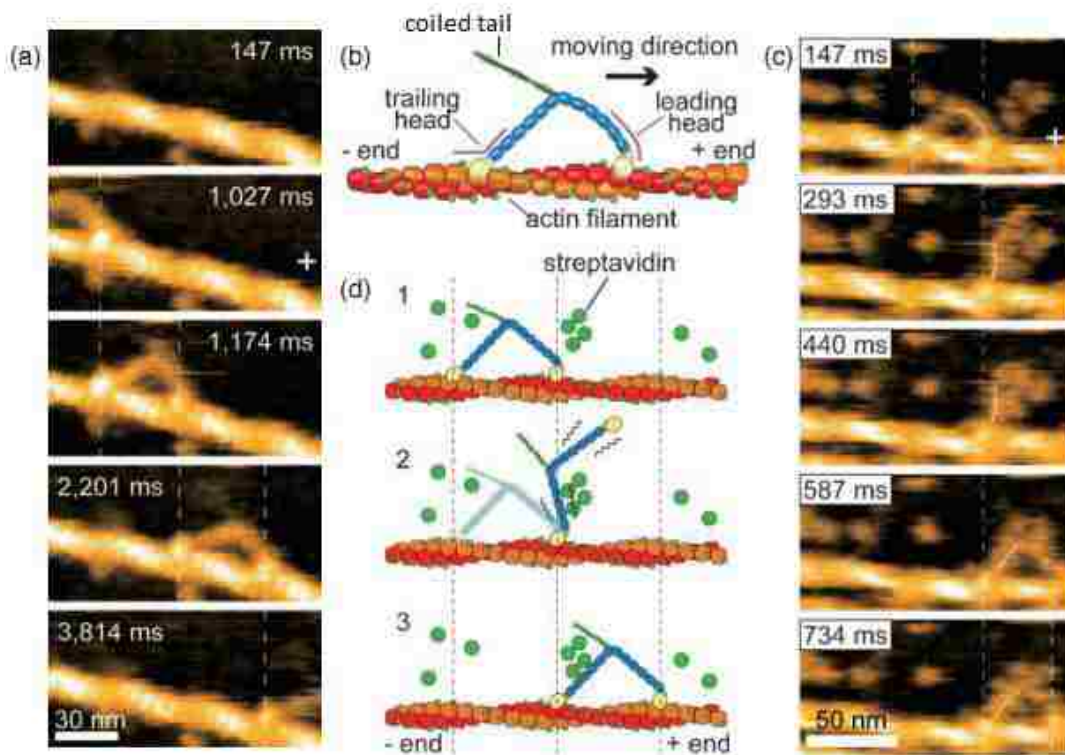Figure 5.7. (49) Walking M5-HMM imaged by HS-AFM in 1μM ATP. (a) AFM images were taken over time (frame rate 7 fps) to show the movement of M5-HlMM across F-actin. (b) An illustration of M5-HMM bound to F-actin at both heads. (c) AFM images were taken over time (frame rate 7 fps) to show hand-over-hand movement. The swinging point is shown by a white line marker. (d) An illustration of the images in c.

Step movement of M5-HMM along F-actin occurs very quickly, and the process was complete within a frame. In order to slow down the steps for imaging, streptavidin molecules were placed on the substrate surface. These molecules served as obstacles to binding, which slowed the rate of movement enough for imaging, as seen in figure 5.7c and illustrated in figure 5.7d. The trailing head detaches from F-actin and the leading head appears to rotate in order to pull the molecule forward. After bypassing the streptavidin molecules, the leading head completes its rotation and the trailing head moves onward to bind at a location farther up the F-actin chain. During this "walk," the trailing head does not interact with the F-actin molecule until it binds and becomes the new leading head. The rotation of the leading head serves as a fulcrum point, in agreement with a proposed mechanism in the literature. (50)

5.3.4. AFM – Conclusion

AFM imaging of ABPs and their interactions with F-actin is a powerful method to study the binding process at the molecular level. With advances in speed and resolution, AFM can provide dynamic and structural information simultaneously.

5.4. Transmission Electron Microscopy

Transmission electron microscopy (TEM) is an imaging technique in which a beam of electrons is transmitted through a sample. After the electrons interact and pass through the sample, they are focused onto a capture device, such as a charge-coupled device, to produce an image. TEM has higher resolution than light microscopes due to the small de Broglie wavelength of electrons, making it an attractive method for studying proteins. Cryogenic freezing is used for biological samples for immobilization and protection from radiation and high vacuum during analysis. (51) Focused ion beam is a milling technique that uses a beam of gallium or helium ions to cut a portion of the specimen for analysis and can be used in sample preparation. (52,53)

Two TEM methods, cryo-electron microscopy and cryo-electron tomography, can be used to study actin and ABPs.

5.4.1 Cryo-Electron Microscopy

Cryo-electron microscopy (cryoEM) is a form of TEM useful to the field of structural biology. Samples are cooled to cryogenic temperatures, usually below -150 °C (123 K). The frozen sample is subjected to a high voltage electron beam that is used to illuminate the specimen and produce an image. In order to obtain the highest resolution possible, distortions inherent from the electron microscope (the contrast transfer function, CTF) are corrected. (54,55) 3D surface maps of an object can be constructed from TEM images taken at varying defoci. (56,57)
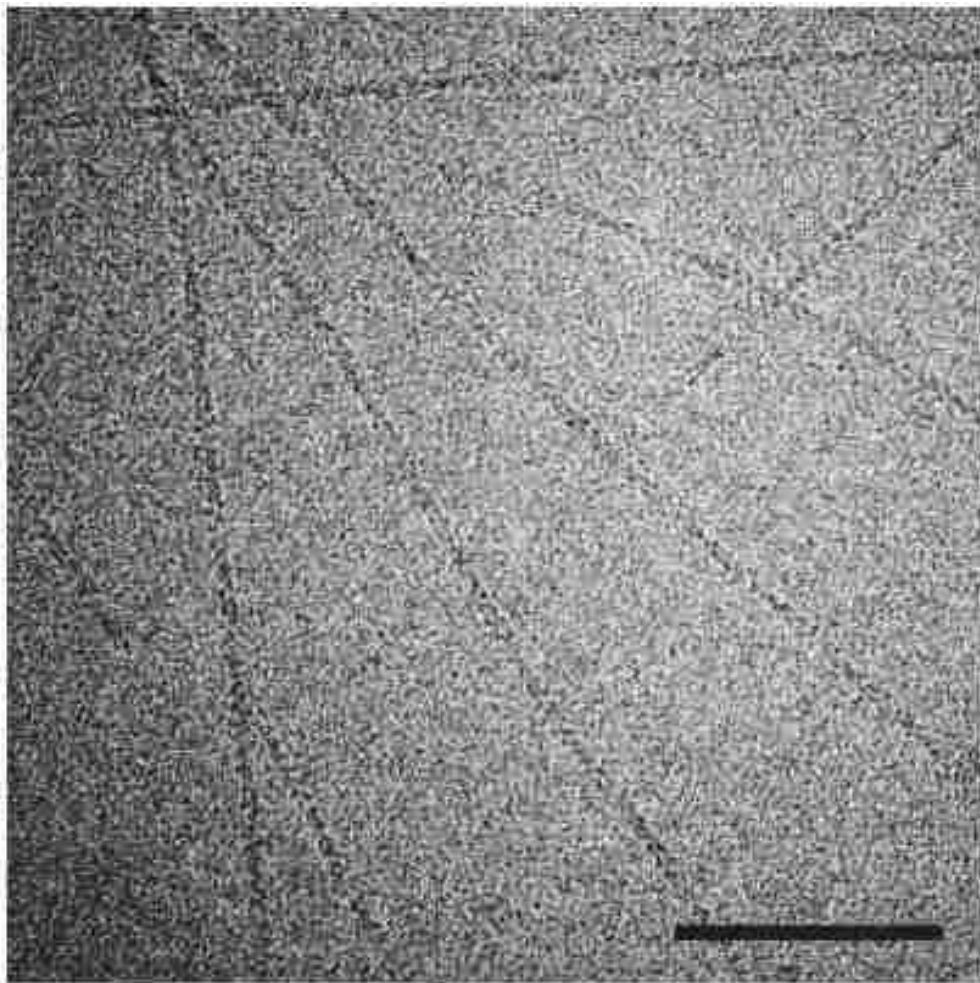
Figure 5.8: (58) High-contrast cryoEM image of F-actin filaments. Scale bar = 100nm.

Before the development of a superfluid helium stage, cryoEM images were limited to a resolution of 13 Å, and (59-61) thin (100 Å diameter), flexible structures like F-actin were difficult to image because of inaccurate image alignment. The superfluid helium stage allows for continuous cooling of samples (62) and improves CTF correction of the electron diffraction pattern. (63) This advancement has allowed for structural analysis of helical, biomolecular assemblies, like F-actin, at near atomic-level resolution. (63-65) In 2010, Takashi Fujii *et al.* used cryoEM to generate a 3D image model of F-actin at 6.6 Å resolution. (66) This study demonstrated the potential of cryoEM to image the secondary structure of smaller, thinner species than had previously been achieved and paved the way for studies of F-actin complexes with ABPs.

5.4.2. Advantages of CryoEM.

Unlike fluorescence microscopic methods, cryoEM samples do not need to be stained or marked in order to be imaged, which allows for species to be viewed directly. Of the methods covered in this review, cryoEM is capable of the highest resolution images of filaments, nearing atomic resolution.

5.4.3. Study: Remodeling of Actin Filaments by ADF/Cofilin Proteins

Using cryoEM, Vitold Gakin *et al.* generated a high-resolution (9 Å) image of F-actin filaments with and without bound cofilin-2. Cofilin/ADF proteins are known modifiers of actin in cells. They regulate actin assembly, including the formation of actin-cofilin rods during neurodegeneration (67) and depolymerization and severing of actin filaments. (68)
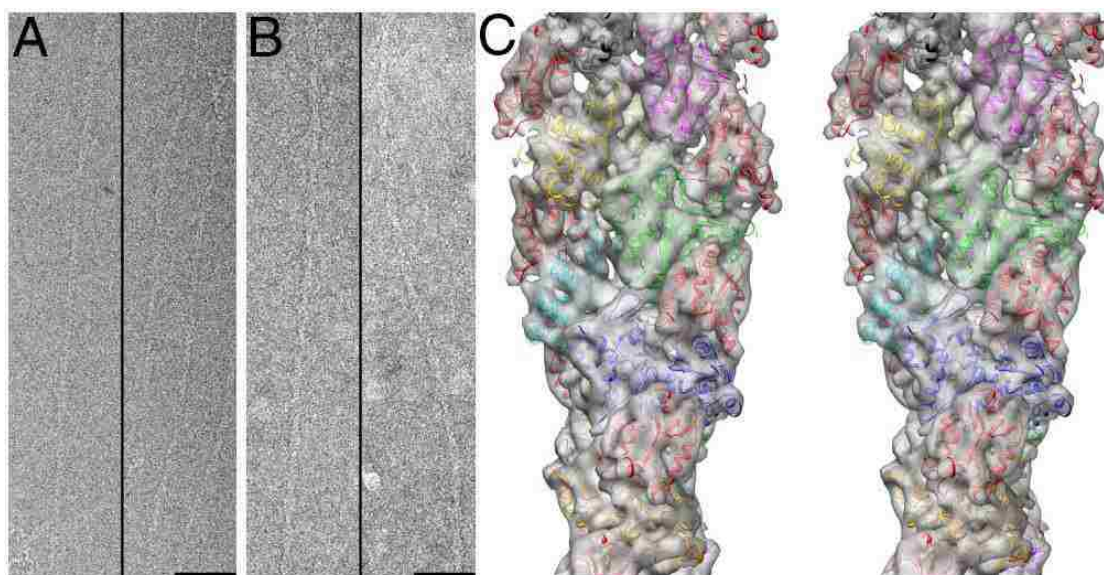
Figure 5.9. (69) CryoEM images of (a) pure F-actin and (b) F-actin decorated with cofilin-2. Scale bar = 500 Å. (c) 3D reconstructed models of F-actin decorated with cofilin-2 (translucent surface). Cofilin molecules are shown in red.

The cryoEM images of F-actin bound with cofilin-2 were used to construct 3D models of the cofilin-decorated F-actin as shown in figure 5.8. Using the models, it was shown that the change in the helical twist of F-actin as induced by cofilin-2 is due to a unique conformation of the F-actin itself. This observation suggests that other ABPs may also cause conformational changes on the same scale, though perhaps in different manners.

5.4.4. Cryo-Electron Tomography

Electron tomography (ET) is a derivative of TEM in which the high voltage electron beam applied to the sample is rotated at various angles about the sample. This technique allows for the construction of 3D images from sectional analysis using many images of the same structure, in contrast to cryoEM, which generates a model from imaging multiple structures. Currently, ET is capable of producing images of biological samples with resolutions in the 5-10 nm range. (70) The technique is also capable of imaging flexible structures and unique features of single particles in a sample. These advantages make ET an appealing candidate for imaging

actin filament networks and actin-ABP complexes. In cryo-electron tomography (cryoET), as in cryo-electron microscopy, the sample is cooled to cryogenic temperatures for analysis.

5.4.5. Speculation: CryoET for the Study of Actin-ABP Complexes

CryoET has already been used extensively for the study of actin filaments and networks, but no studies of actin-ABP interactions were found. The Hanein lab has performed numerous studies of actin using cryoET and written several good reviews on the subject. (71,72) CryoET would be useful for studying actin-ABP complexes because 3D volumes can be produced for unique features such as branching, cross-linking, and overlapping of filaments in networks. (73) The primary limitation of cryoET compared to cryoEM for the study of protein complexes is the relatively low resolution. A new approach to improving the final resolution is sub-volume averaging, where multiple structures are imaged, aligned, and averaged. (74,75) Actin-ABP complexes should be a good candidate for sub-volume averaging since multiple ABP molecules can bind along one F-actin filament.

5.4.6 TEM – Conclusion

Recent advances have made cryoEM a viable method to study thin filaments in biological systems. CryoEM paired with 3D reconstruction software has been used to visualize the structure of F-actin and its complex with cofilin-2. Future studies will aid our understanding of F-actin structural changes in the presence of ABPs. CryoET's ability to analyze sections of sample at varying rotations and construct a 3D image from the data collected make it a powerful tool. However, a major disadvantage of TEM methods, especially of cryoET, is the poor signal-to-noise ratio, which is difficult to overcome when there is a need to minimize radiation damage to the sample. (76) It is possible that as higher resolution electron microscopy and tomography

methods become available, it will be possible to obtain "snapshots" of structural processes such as binding, polymerization, or depolymerization of actin filaments.

5.5. Looking Forward: Correlative Light/Electron Microscopy

In the past decade, there has been an increased interest in combining both light and electron microscopy methods in order to exploit the advantages of both techniques. Light microscopy allows for rapid screening of a large area, and electron microscopy produces images at a higher resolution than light microscopy methods. Correlative light/electron microscopy (CLEM) was first used in the 1970s to study stained cells in tissue samples by coupling light immunohistological cell staining with electron microscopy. (77) With CLEM, the sample is cooled to cryogenic temperatures, aligned to a grid, and imaged with light microscopy, typically fluorescence microscopy. Areas of interest are identified and their coordinates on the sample grid are recorded and relayed to the electron microscope for imaging. Since navigation to the areas of interest is streamlined, pre-irradiation and damage of the sample are minimized. (76) CLEM also allows for a direct correlation between data collected using both methods, which aids in image interpretation. The primary limitation of CLEM is the specialized nature of the technique, which requires multiple, expensive instruments and the software and expertise to interface them.

CLEM has not been used to study actin-ABP complexes, but has advantages specific to such systems. In particular, CLEM is well-suited for cryoET sub-volume averaging approaches. With a fluorescently labeled ABP, CLEM could be used to quickly identify bound ABP and direct cryoET imaging of multiple complexes.

5.6. Discussion

Images of F-actin and ABP interactions provide information about the binding process, such as alteration of the helical twist, ABP dynamics, physical bending of filaments, and network

assembly dynamics. These mechanistic details of actin and ABPs are crucial to understand the function of the F-actin networks within cells.

Fluorescence microscopy (FSM and TIRFM) and atomic force microscopy can be used to generate time-lapse images of binding and dynamics. Visual data can be easily interpreted and explain physical occurrences within the sample. Additionally, both methods can be quantitative, providing numerical data to supplement visual evidence. While fluorescence microscopy is widespread, cheaper, and very efficient for the study of structural proteins, F-actin does not autofluoresce and requires sample preparation. Since only fluorescent molecules are imaged, fluorescence microscopy provides a level of specificity in imaging that is difficult to obtain with other forms of microscopy. AFM does not require sample preparation beyond immobilization, but the high cost of AFM remains a limitation to study F-actin.

Advances in cryo-electron microscopy and tomography now allow for detailed visualization of actin filaments. There is also no need for marking, staining, or dyeing of the sample. Electron microscopy methods are the highest resolution techniques available to image F-actin and its complexes. We anticipate that cryo-ET sub-volume averaging, possibly implemented as a CLEM technique, will improve the 3D resolution imaging of actin-ABP complexes and advance our knowledge about the role of ABP's in cells.

5.7. References

1.   Doherty, G. J., and McMahon, H. T. (2008) Mediation, modulation, and consequences of membrane-cytoskeleton interactions. *Annu. Rev. Biophys.* **37**, 65-95

2.   Dos Remedios, C. G., Chhabra, D., Kekic, M., Dedova, I. V., Tsubakihara, M., Berry, D. A., and Nosworthy, N. J. (2003) Actin binding proteins: regulation of cytoskeletal microfilaments. *Physiol. Rev.* **83**, 433-473

3.   Winder, S. J., and Ayscough, K. R. (2005) Actin-binding proteins. *J. Cell Sci.* **118**, 651-654

4. Carugo, K. D., Banuelos, S., and Saraste, M. (1997) Crystal structure of a calponin homology domain. *Nat. Struct. Mol. Biol.* **4**, 175-179

5. Korenbaum, E., and Rivero, F. (2002) Calponin homology domains at a glance. *J. Cell Sci.* **115**, 3543-3545

6. Pollard, T. D., and Korn, E. D. (1973) Acanthamoeba Myosin II interaction with actin and with a new cofactor protein required for actin activation of Mg2+ adenosine triphosphate activity. *J. Biol. Chem.* **248**, 4691-4697

7. Miller, K. G., and Alberts, B. M. (1989) F-actin affinity chromatography: technique for isolating previously unidentified actin-binding proteins. *Proc. Natl. Acad. Sci. U. S. A.* **86**, 4808-4812

8. Waterman-Storer, C. M., Desai, A., Chloe Bulinski, J., and Salmon, E. D. (1998) Fluorescent speckle microscopy, a method to visualize the dynamics of protein assemblies in living cells. *Curr. Biol.* **8**, 1227-1230

9. Danuser, G., and Waterman-Storer, C. M. (2003) Quantitative fluorescent speckle microscopy: where it came from and where it is going. *J. Microsc.* **211**, 191–207

10. Wang, Y.-L. (1988) Chapter 1: Fluorescent analog cytochemistry: tracing functional protein components in living cells. in *Methods in Cell Biology* (Yu-Li Wang, D. L. T., and Jeon, K. W. eds.), Academic Press. pp 1-12

11. Waterman-Storer, C. M., and Salmon, E. D. (1998) How microtubules get fluorescent speckles. *Biophys. J.* **75**, 2059-2069

12. Waterman-Storer, C. M., and Danuser, G. (2002) New directions for fluorescent speckle microscopy. *Curr. Biol.* **12**, R633-R640

13. Danuser, G., and Waterman-Storer, C. M. (2006) Quantitative fluorescent speckle microscopy of cytoskeleton dynamics. *Annu. Rev. Biophys. Biomol. Struct.* **35**, 361-387

14. Salmon, W. C., Adams, M. C., and Waterman-Storer, C. M. (2002) Dual-wavelength fluorescent speckle microscopy reveals coupling of microtubule and actin movements in migrating cells. *J. Cell Biol.* **158**, 31-37

15. Gupton, S. L., Anderson, K. L., Kole, T. P., Fischer, R. S., Ponti, A., Hitchcock-DeGregori, S. E., Danuser, G., Fowler, V. M., Wirtz, D., Hanein, D., and Waterman-Storer, C. M. (2005) Cell migration without a lamellipodium: translation of actin dynamics into cell movement mediated by tropomyosin. *J. Cell Biol.* **168**, 619-631

16. Ponti, A., Machacek, M., Gupton, S. L., Waterman-Storer, C. M., and Danuser, G. (2004) Two distinct actin networks drive the protrusion of migrating cells. *Science* **305**, 1782-1786

17. Ponti, A., Matov, A., Adams, M., Gupton, S., Waterman-Storer, C. M., and Danuser, G. (2005) Periodic patterns of actin turnover in lamellipodia and lamellae of migrating epithelial cells analyzed by quantitative fluorescent speckle microscopy. *Biophys. J.* **89**, 3456-3469

18. Reprinted from Biophysical Journal, 89, A. Ponti, A. Matov, M. Adams, S. Gupton, C. M. Waterman-Storer, and G. Danuser, Periodic patterns of actin turnover in lamellipodia and lamellae of migrating epithelial cells analyzed by quantitative fluorescent speckle microscopy, 3466, Copyright (2005), with permission from Elsevier.

19. Axelrod, D. (1981) Cell-substrate contacts illuminated by total internal reflection fluorescence. *J. Cell Biol.* **89**, 141-145

20. Gardner, M. K., Charlebois, B. D., Jánosi, I. M., Howard, J., Hunt, A. J., and Odde, D. J. (2011) Rapid microtubule self-assembly kinetics. *Cell* **146**, 582-592

21. Caporizzo, M. A., Sun, Y., Goldman, Y. E., and Composto, R. J. (2012) Nanoscale topography mediates the adhesion of F-actin. *Langmuir* **28**, 12216-12224

22. Kovar, D. R., and Pollard, T. D. (2004) Insertional assembly of actin filament barbed ends in association with formins produces piconewton forces. *Proc. Natl. Acad. Sci. U. S. A.* **101**, 14725-14730

23. Helfer, E. (2010) Visualization of individual actin filament assembly. in *Actin-Based Motility*, Springer, Van Godewijckstraat. pp 317-333

24. Ramabhadran, V., Gurel, P. S., and Higgs, H. N. (2012) Mutations to the formin homology 2 domain of INF2 protein have unexpected effects on actin polymerization and severing. *J. Biol. Chem.* **287**, 34234-34245

25. Mogilner, A., and Oster, G. (2003) Force generation by actin polymerization II: the elastic ratchet and tethered filaments. *Biophys. J.* **84**, 1591-1605

26. Carlier, M.-F., Clainche, C. L., Wiesner, S., and Pantaloni, D. (2003) Actin-based motility: from molecules to movement. *BioEssays* **25**, 336-345

27. Howard, J. (2002) Mechanics of motor proteins. in *Physics of Bio-Molecules and Cells* (Flyvbjerg, F., Jülicher, F., Ormos, P., and David, F. eds.), Springer Berlin - Heidelberg, Berlin. pp 69-94

28. Heintzmann, R., and Ficz, G. (2006) Breaking the resolution limit in light microscopy. *Briefings Funct. Genomics Proteomics* **5**, 289-301

29. Karrasch, S., Hegerl, R., Hoh, J. H., Baumeister, W., and Engel, A. (1994) Atomic force microscopy produces faithful high-resolution images of protein surfaces in an aqueous environment. *Proc. Natl. Acad. Sci. U. S. A.* **91**, 836-838

30. Binnig, G., Quate, C. F., and Gerber, C. (1986) Atomic force microscope. *Phys. Rev. Lett.* **56**, 930-933

31. Gould, S., Marti, O., Drake, B., Hellemans, L., Bracker, C. E., Hansma, P. K., Keder, N. L., Eddy, M. M., and Stucky, G. D. (1988) Molecular resolution images of amino acid crystals with the atomic force microscope. *Nature* **332**, 332-334

32. Walters, D. A., Cleveland, J. P., Thomson, N. H., Hansma, P. K., Wendman, M. A., Gurley, G., and Elings, V. (1996) Short cantilevers for atomic force microscopy. *Rev. Sci. Instrum.* **67**, 3583-3590

33. Ando, T., Kodera, N., Takai, E., Maruyama, D., Saito, K., and Toda, A. (2001) A high-speed atomic force microscope for studying biological macromolecules. *Proc. Natl. Acad. Sci. U. S. A.* **98**, 12468-12472

34. Kodera, N., Yamamoto, D., Ishikawa, R., and Ando, T. (2010) Video imaging of walking myosin V by high-speed atomic force microscopy. *Nature* **468**, 72-76

35. Sharma, S., Grintsevich, E. E., Phillips, M. L., Reisler, E., and Gimzewski, J. K. (2011) Atomic force microscopy reveals drebrin induced remodeling of f-actin with subnanometer resolution. *Nano Lett.* **11**, 825-827

36. Shao, Z., Shi, D., and Somlyo, A. V. (2000) Cryoatomic force microscopy of filamentous actin. *Biophys. J.* **78**, 950-958

37. Reprinted (adapted) with permission from S. Sharma, E.E. Grintsevich, M.L. Phillips, E. Reisler, and J.K. Gimzewski, Atomic force microscopy reveals drebrin induced remodeling of F-actin with subnanometer resolution. Nano Lett. 11 (2011) 825-827. Copyright (2011) American Chemical Society.

38. McGough, A., Pope, B., Chiu, W., and Weeds, A. (1997) Cofilin changes the twist of F-actin: implications for actin filament dynamics and cellular function. *J. Cell Biol.* **138**, 771-781

39. Frontali, C., Dore, E., Ferrauto, A., Gratton, E., Bettini, A., Pozzan, M. R., and Valdevit, E. (1979) An absolute method for the determination of the persistence length of native DNA from electron micrographs. *Biopolymers* **18**, 1353-1373

40. Takebayashi, T., Morita, Y., and Oosawa, F. (1977) Electron microscopic investigation of the flexibility of F-actin. *Biochim. Biophys. Acta, Protein Struct.* **492**, 357-363

41. Ishikawa, R., Hayashi, K., Shirao, T., Xue, Y., Takagi, T., Sasaki, Y., and Kohama, K. (1994) Drebrin, a development-associated brain protein from rat embryo, causes the dissociation of tropomyosin from actin filaments. *J. Biol. Chem.* **269**, 29928-29933

42. Isambert, H., Venier, P., Maggs, A., Fattoum, A., Kassab, R., Pantaloni, D., and Carlier, M. (1995) Flexibility of actin filaments derived from thermal fluctuations. Effect of

bound nucleotide, phalloidin, and muscle regulatory proteins. *J. Biol. Chem.* **270**, 11437-11444

43.   Sakamoto, T., Webb, M. R., Forgacs, E., White, H. D., and Sellers, J. R. (2008) Direct observation of the mechanochemical coupling in myosin Va during processive movement. *Nature* **455**, 128-132

44.   Mehta, A. D., Rock, R. S., Rief, M., Spudich, J. A., Mooseker, M. S., and Cheney, R. E. (1999) Myosin-V is a processive actin-based motor. *Nature* **400**, 590-593

45.   Yildiz, A., Forkey, J. N., McKinney, S. A., Ha, T., Goldman, Y. E., and Selvin, P. R. (2003) Myosin V walks hand-over-hand: single fluorophore imaging with 1.5-nm localization. *Science* **300**, 2061-2065

46.   Forkey, J. N., Quinlan, M. E., Alexander Shaw, M., Corrie, J. E. T., and Goldman, Y. E. (2003) Three-dimensional structural dynamics of myosin V by single-molecule fluorescence polarization. *Nature* **422**, 399-404

47.   Warshaw, D. M., Kennedy, G. G., Work, S. S., Krementsova, E. B., Beck, S., and Trybus, K. M. (2005) Differential labeling of myosin V heads with quantum dots allows direct visualization of hand-over-hand processivity. *Biophys. J.* **88**, L30-L32

48.   Ando, T., Uchihashi, T., and Kodera, N. (2012) High-speed atomic force microscopy. *Jpn. J. Appl. Phys.* **51**, 08KA021-008KA0215

49.   Adapted by permission from Macmillan Publishers Ltd: Nature (N. Kodera, D. Yamamoto, R. Ishikawa, and T. Ando, Video imaging of walking myosin V by high-speed atomic force microscopy. Nature 468 (2010) 72-76.), copyright (2010)

50.   Huxley, H. E. (1969) The mechanism of muscular contraction. *Science* **164**, 1356-1366

51.   Adrian, M., Dubochet, J., Lepault, J., and McDowall, A. W. (1984) Cryo-electron microscopy of viruses. *Nature* **308**, 32-36

52.   Osumi, M. (2012) Visualization of yeast cells by electron microscopy. *J. Electron Microsc. (Tokyo)* **61**, 343-365

53.   Suzuki, M., Asada, Y., Watanabe, D., and Ohya, Y. (2004) Cell shape and growth of budding yeast cells in restrictive microenvironments. *Yeast (Chichester, England)* **21**, 983-989

54.   Mindell, J. A., and Grigorieff, N. (2003) Accurate determination of local defocus and specimen tilt in electron microscopy. *J. Struct. Biol.* **142**, 334-347

55.   Ludtke, S. J., Baldwin, P. R., and Chiu, W. (1999) EMAN: semiautomated software for high-resolution single-particle reconstructions. *J. Struct. Biol.* **128**, 82-97

56.   Stewart, P. L., Fuller, S. D., and Burnett, R. M. (1993) Difference imaging of adenovirus: bridging the resolution gap between X-ray crystallography and electron microscopy. *The EMBO journal* **12**, 2589-2599

57.   Penczek, P. A., Zhu, J., Schröder, R., and Frank, J. (1997) Three domensional reconstruction with contrast transfer function compensation from defocus series. *Scanning Microscopy* **11**, 147-154

58.   Reprinted by permission from Macmillan Publishers Ltd: Nature (T. Fujii, A.H. Iwane, T. Yanagida, and K. Namba, Direct visualization of secondary structures of F-actin by electron cryomicroscopy. Nature 467 (2010) 724-728), copyright (2010)

59.   Oda, T., Iwasa, M., Aihara, T., Maeda, Y., and Narita, A. (2009) The nature of the globular- to fibrous-actin transition. *Nature* **457**, 441-445

60.   Galkin, V. E., Orlova, A., Cherepanova, O., Lebart, M.-C., and Egelman, E. H. (2008) High-resolution cryo-EM structure of the F-actin–fimbrin/plastin ABD2 complex. *Proc. Natl. Acad. Sci. U. S. A.* **105**, 1494-1498

61.   Holmes, K. C., Angert, I., Jon Kull, F., Jahn, W., and Schroder, R. R. (2003) Electron cryo-microscopy shows how strong binding of myosin to actin releases nucleotide. *Nature* **425**, 423-427

62.   Fujiyoshi, Y., Mizusaki, T., Morikawa, K., Yamagishi, H., Aoki, Y., Kihara, H., and Harada, Y. (1991) Development of a superfluid helium stage for high-resolution electron microscopy. *Ultramicroscopy* **38**, 241-251

63.   Sachse, C., Chen, J. Z., Coureux, P. D., Stroupe, M. E., Fandrich, M., and Grigorieff, N. (2007) High-resolution electron microscopy of helical specimens: a fresh look at tobacco mosaic virus. *J. Mol. Biol.* **371**, 812-835

64.   Yonekura, K., Maki-Yonekura, S., and Namba, K. (2003) Complete atomic model of the bacterial flagellar filament by electron cryomicroscopy. *Nature* **424**, 643-650

65.   Miyazawa, A., Fujiyoshi, Y., and Unwin, N. (2003) Structure and gating mechanism of the acetylcholine receptor pore. *Nature* **423**, 949-955

66.   Fujii, T., Iwane, A. H., Yanagida, T., and Namba, K. (2010) Direct visualization of secondary structures of F-actin by electron cryomicroscopy. *Nature* **467**, 724-728

67.   Bamburg, J. R., Bernstein, B. W., Davis, R. C., Flynn, K. C., Goldsbury, C., Jensen, J. R., Maloney, M. T., Marsden, I. T., Minamide, L. S., Pak, C. W., Shaw, A. E., Whiteman, I., and Wiggan, O. (2010) ADF/Cofilin-actin rods in neurodegenerative diseases. *Curr. Alzheimer Res.* **7**, 241-250

68.   McCullough, B. R., Blanchoin, L., Martiel, J.-L., and De La Cruz, E. M. (2008) Cofilin increases the bending flexibility of actin filaments: implications for severing and cell mechanics. *J. Mol. Biol.* **381**, 550-558

69. Galkin, V. E., Orlova, A., Kudryashov, D. S., Solodukhin, A., Reisler, E., Schröder, G. F., and Egelman, E. H. (2011) Remodeling of actin filaments by ADF/cofilin proteins. *Proc. Natl. Acad. Sci. U. S. A.* **108**, 20568-20572

70. Diebolder, C. A., Koster, A. J., and Koning, R. I. (2012) Pushing the resolution limits in cryo electron tomography of biological structures. *J. Microsc.* **248**, 1-5

71. Hanein, D. (2010) Chapter Ten - Tomography of Actin Cytoskeletal Networks. in *Methods in enzymology* (Grant, J. J. ed.), Academic Press. pp 203-214

72. van der Heide, P., Xu, X.-P., Marsh, B. J., Hanein, D., and Volkmann, N. (2007) Efficient automatic noise reduction of electron tomographic reconstructions based on iterative median filtering. *J. Struct. Biol.* **158**, 196-204

73. Urban, E., Jacob, S., Nemethova, M., Resch, G. P., and Small, J. V. (2010) Electron tomography reveals unbranched networks of actin filaments in lamellipodia. *Nat. Cell Biol.* **12**, 429-435

74. Bartesaghi, A., Sprechmann, P., Liu, J., Randall, G., Sapiro, G., and Subramaniam, S. (2008) Classification and 3D averaging with missing wedge correction in biological electron tomography. *J. Struct. Biol.* **162**, 436-450

75. Bartesaghi, A., and Subramaniam, S. (2009) Membrane protein structure determination using cryo-electron tomography and 3D image averaging. *Curr. Opin. Struct. Biol.* **19**, 402-407

76. Sartori, A., Gatz, R., Beck, F., Rigort, A., Baumeister, W., and Plitzko, J. M. (2007) Correlative microscopy: Bridging the gap between fluorescence light microscopy and cryo-electron tomography. *J. Struct. Biol.* **160**, 135-145

77. Kobayashi, S., Serizawa, Y., Fujita, T., and Coupland, R. E. (1978) SGC (Small granule chromaffin) cells in the mouse adrenal medulla - light and electron microscopic identification using semi-thin and ultra-thin sections. *Endocrinol. Jpn.* **25**, 467-476

APPENDIX

A1. Letter of Permission – Elsevir License Terms and Conditions

This is a License Agreement between Maggie Thomasson ("You") and Elsevier ("Elsevier") provided by Copyright Clearance Center ("CCC"). The license consists of your order details, the terms and conditions provided by Elsevier, and the payment terms and conditions.

All payments must be made in full to CCC. For payment instructions, please see information listed at the bottom of this form.

Supplier	Elsevier Limited The Boulevard,Langford Lane Kidlington,Oxford,OX5 1GB,UK
Registered Company Number	1982084
Customer name	Maggie Thomasson
Customer address	427 Choppin Hall
	Baton Rouge, LA 70820
License number	3853760676239
License date	Apr 21, 2016
Licensed content publisher	Elsevier
Licensed content publication	Analytical Biochemistry
Licensed content title	Microscopy basics and the study of actin–actin-binding protein interactions
Licensed content author	Maggie S. Thomasson,Megan A. Macnaughtan
Licensed content date	15 December 2013
Licensed content volume number	443
Licensed content issue number	2
Number of pages	10
Start Page	156
End Page	165
Type of Use	reuse in a thesis/dissertation
Portion	full article
Format	both print and electronic

Are you the author of this Elsevier article?	Yes
Will you be translating?	No
Title of your thesis/dissertation	INVESTIGATING THE STRUCTURE OF THE PAPAIN-INHIBITOR COMPLEX USING PRE-NMR AND SPR
Expected completion date	Aug 2016
Estimated size (number of pages)	40
Elsevier VAT number	GB 494 6272 12
Permissions price	0.00 USD
VAT/Local Sales Tax	0.00 USD / 0.00 GBP
Total	0.00 USD
Terms and Conditions	

INTRODUCTION

1. The publisher for this copyrighted material is Elsevier. By clicking "accept" in connection with completing this licensing transaction, you agree that the following terms and conditions apply to this transaction (along with the Billing and Payment terms and conditions established by Copyright Clearance Center, Inc. ("CCC"), at the time that you opened your Rightslink account and that are available at any time at http://myaccount.copyright.com).

GENERAL TERMS

2. Elsevier hereby grants you permission to reproduce the aforementioned material subject to the terms and conditions indicated.

3. Acknowledgement: If any part of the material to be used (for example, figures) has appeared in our publication with credit or acknowledgement to another source, permission must also be sought from that source. If such permission is not obtained then that material may not be included in your publication/copies. Suitable acknowledgement to the source must be made, either as a footnote or in a reference list at the end of your publication, as follows:

"Reprinted from Publication title, Vol /edition number, Author(s), Title of article / title of chapter, Pages No., Copyright (Year), with permission from Elsevier [OR APPLICABLE SOCIETY COPYRIGHT OWNER]." Also Lancet special credit - "Reprinted from The Lancet, Vol. number, Author(s), Title of article, Pages No., Copyright (Year), with permission from Elsevier."

4. Reproduction of this material is confined to the purpose and/or media for which permission is hereby given.

5. Altering/Modifying Material: Not Permitted. However figures and illustrations may be altered/adapted minimally to serve your work. Any other abbreviations, additions, deletions and/or any other alterations shall be made only with prior written authorization of Elsevier Ltd. (Please contact Elsevier at permissions@elsevier.com)

6. If the permission fee for the requested use of our material is waived in this instance, please be advised that your future requests for Elsevier materials may attract a fee.

7. Reservation of Rights: Publisher reserves all rights not specifically granted in the combination of (i) the license details provided by you and accepted in the course of this licensing transaction, (ii) these terms and conditions and (iii) CCC's Billing and Payment terms and conditions.

8. License Contingent Upon Payment: While you may exercise the rights licensed immediately upon issuance of the license at the end of the licensing process for the transaction, provided that you have disclosed complete and accurate details of your proposed use, no license is finally effective unless and until full payment is received from you (either by publisher or by CCC) as provided in CCC's Billing and Payment terms and conditions. If full payment is not received on a timely basis, then any license preliminarily granted shall be deemed automatically revoked and shall be void as if never granted. Further, in the event that you breach any of these terms and conditions or any of CCC's Billing and Payment terms and conditions, the license is automatically revoked and shall be void as if never granted. Use of materials

73

as described in a revoked license, as well as any use of the materials beyond the scope of an unrevoked license, may constitute copyright infringement and publisher reserves the right to take any and all action to protect its copyright in the materials.

9. Warranties: Publisher makes no representations or warranties with respect to the licensed material.

10. Indemnity: You hereby indemnify and agree to hold harmless publisher and CCC, and their respective officers, directors, employees and agents, from and against any and all claims arising out of your use of the licensed material other than as specifically authorized pursuant to this license.

11. No Transfer of License: This license is personal to you and may not be sublicensed, assigned, or transferred by you to any other person without publisher's written permission.

12. No Amendment Except in Writing: This license may not be amended except in a writing signed by both parties (or, in the case of publisher, by CCC on publisher's behalf).

13. Objection to Contrary Terms: Publisher hereby objects to any terms contained in any purchase order, acknowledgment, check endorsement or other writing prepared by you, which terms are inconsistent with these terms and conditions or CCC's Billing and Payment terms and conditions. These terms and conditions, together with CCC's Billing and Payment terms and conditions (which are incorporated herein), comprise the entire agreement between you and publisher (and CCC) concerning this licensing transaction. In the event of any conflict between your obligations established by these terms and conditions and those established by CCC's Billing and Payment terms and conditions, these terms and conditions shall control.

14. Revocation: Elsevier or Copyright Clearance Center may deny the permissions described in this License at their sole discretion, for any reason or no reason, with a full refund payable to you. Notice of such denial will be made using the contact information provided by you. Failure to receive such notice will not alter or invalidate the denial. In no event will Elsevier or Copyright Clearance Center be responsible or liable for any costs, expenses or damage incurred by you as a result of a denial of your permission request, other than a refund of the amount(s) paid by you to Elsevier and/or Copyright Clearance Center for denied permissions.

<div align="center">

LIMITED LICENSE

</div>

The following terms and conditions apply only to specific license types:

15. **Translation**: This permission is granted for non-exclusive world **English** rights only unless your license was granted for translation rights. If you licensed translation rights you may only translate this content into the languages you requested. A professional translator must perform all translations and reproduce the content word for word preserving the integrity of the article.

16. **Posting licensed content on any Website**: The following terms and conditions apply as follows: Licensing material from an Elsevier journal: All content posted to the web site must maintain the copyright information line on the bottom of each image; A hyper-text must be included to the Homepage of the journal from which you are licensing at http://www.sciencedirect.com/science/journal/xxxxx or the Elsevier homepage for books at http://www.elsevier.com; Central Storage: This license does not include permission for a scanned version of the material to be stored in a central repository such as that provided by Heron/XanEdu.

Licensing material from an Elsevier book: A hyper-text link must be included to the Elsevier homepage at http://www.elsevier.com . All content posted to the web site must maintain the copyright information line on the bottom of each image.

Posting licensed content on Electronic reserve: In addition to the above the following clauses are applicable: The web site must be password-protected and made available only to bona fide students registered on a relevant course. This permission is granted for 1 year only. You may obtain a new license for future website posting.

17. **For journal authors:** the following clauses are applicable in addition to the above:

Preprints:

A preprint is an author's own write-up of research results and analysis, it has not been peer-reviewed, nor has it had any other value added to it by a publisher (such as formatting, copyright, technical enhancement etc.).

Authors can share their preprints anywhere at any time. Preprints should not be added to or enhanced in any way in order to appear more like, or to substitute for, the final versions of articles however authors can update their preprints on arXiv or RePEc with their Accepted Author Manuscript (see below).

If accepted for publication, we encourage authors to link from the preprint to their formal publication via its DOI. Millions of researchers have access to the formal publications on ScienceDirect, and so links will help users to find, access, cite and use the best available version. Please note that Cell Press, The Lancet and some society-owned have different preprint policies. Information on these policies is available on the journal homepage.

Accepted Author Manuscripts: An accepted author manuscript is the manuscript of an article that has been accepted for publication and which typically includes author-incorporated changes suggested during submission, peer review and editor-author communications.

Authors can share their accepted author manuscript:

- – immediately
  - o via their non-commercial person homepage or blog
  - o by updating a preprint in arXiv or RePEc with the accepted manuscript
  - o via their research institute or institutional repository for internal institutional uses or as part of an invitation-only research collaboration work-group
  - o directly by providing copies to their students or to research collaborators for their personal use
  - o for private scholarly sharing as part of an invitation-only work group on commercial sites with which Elsevier has an agreement
- – after the embargo period
  - o via non-commercial hosting platforms such as their institutional repository
  - o via commercial sites with which Elsevier has an agreement

In all cases accepted manuscripts should:

- – link to the formal publication via its DOI
- – bear a CC-BY-NC-ND license - this is easy to do
- – if aggregated with other manuscripts, for example in a repository or other site, be shared in alignment with our hosting policy not be added to or enhanced in any way to appear more like, or to substitute for, the published journal article.

Published journal article (JPA): A published journal article (PJA) is the definitive final record of published research that appears or will appear in the journal and embodies all value-adding publishing activities including peer review co-ordination, copy-editing, formatting, (if relevant) pagination and online enrichment.

Policies for sharing publishing journal articles differ for subscription and gold open access articles:

Subscription Articles: If you are an author, please share a link to your article rather than the full-text. Millions of researchers have access to the formal publications on ScienceDirect, and so links will help your users to find, access, cite, and use the best available version.

Theses and dissertations which contain embedded PJAs as part of the formal submission can be posted publicly by the awarding institution with DOI links back to the formal publications on ScienceDirect.

If you are affiliated with a library that subscribes to ScienceDirect you have additional private sharing rights for others' research accessed under that agreement. This includes use for classroom teaching and internal training at the institution (including use in course packs and courseware programs), and inclusion of the article for grant funding purposes.

Gold Open Access Articles: May be shared according to the author-selected end-user license and should contain a [CrossMark logo](), the end user license, and a DOI link to the formal publication on ScienceDirect. Please refer to Elsevier's [posting policy]() for further information.

18. **For book authors** the following clauses are applicable in addition to the above: Authors are permitted to place a brief summary of their work online only. You are not allowed to download and post the published electronic version of your chapter, nor may you scan the printed edition to create an electronic version. **Posting to a repository:** Authors are permitted to post a summary of their chapter only in their institution's repository.

19. **Thesis/Dissertation**: If your license is for use in a thesis/dissertation your thesis may be submitted to your institution in either print or electronic form. Should your thesis be published commercially, please reapply for permission. These requirements include permission for the Library and Archives of Canada to supply single copies, on demand, of the complete thesis and include permission for Proquest/UMI to supply single copies, on demand, of the complete thesis. Should your thesis be published commercially, please reapply for permission. Theses and dissertations which contain embedded PJAs as part of the formal

submission can be posted publicly by the awarding institution with DOI links back to the formal publications on ScienceDirect.

Elsevier Open Access Terms and Conditions

You can publish open access with Elsevier in hundreds of open access journals or in nearly 2000 established subscription journals that support open access publishing. Permitted third party re-use of these open access articles is defined by the author's choice of Creative Commons user license. See our open access license policy for more information.

Terms & Conditions applicable to all Open Access articles published with Elsevier:

Any reuse of the article must not represent the author as endorsing the adaptation of the article nor should the article be modified in such a way as to damage the author's honour or reputation. If any changes have been made, such changes must be clearly indicated.

The author(s) must be appropriately credited and we ask that you include the end user license and a DOI link to the formal publication on ScienceDirect.

If any part of the material to be used (for example, figures) has appeared in our publication with credit or acknowledgement to another source it is the responsibility of the user to ensure their reuse complies with the terms and conditions determined by the rights holder.

Additional Terms & Conditions applicable to each Creative Commons user license:

CC BY: The CC-BY license allows users to copy, to create extracts, abstracts and new works from the Article, to alter and revise the Article and to make commercial use of the Article (including reuse and/or resale of the Article by commercial entities), provided the user gives appropriate credit (with a link to the formal publication through the relevant DOI), provides a link to the license, indicates if changes were made and the licensor is not represented as endorsing the use made of the work. The full details of the license are available at http://creativecommons.org/licenses/by/4.0.

CC BY NC SA: The CC BY-NC-SA license allows users to copy, to create extracts, abstracts and new works from the Article, to alter and revise the Article, provided this is not done for commercial purposes, and that the user gives appropriate credit (with a link to the formal publication through the relevant DOI), provides a link to the license, indicates if changes were made and the licensor is not represented as endorsing the use made of the work. Further, any new works must be made available on the same conditions. The full details of the license are available at http://creativecommons.org/licenses/by-nc-sa/4.0.

CC BY NC ND: The CC BY-NC-ND license allows users to copy and distribute the Article, provided this is not done for commercial purposes and further does not permit distribution of the Article if it is changed or edited in any way, and provided the user gives appropriate credit (with a link to the formal publication through the relevant DOI), provides a link to the license, and that the licensor is not represented as endorsing the use made of the work. The full details of the license are available at http://creativecommons.org/licenses/by-nc-nd/4.0. Any commercial reuse of Open Access articles published with a CC BY NC SA or CC BY NC ND license requires permission from Elsevier and will be subject to a fee.

Commercial reuse includes:

- – Associating advertising with the full text of the Article
- – Charging fees for document delivery or access
- – Article aggregation
- – Systematic distribution via e-mail lists or share buttons

Posting or linking by commercial companies for use by customers of those companies.

20. **Other Conditions**:

v1.8

Questions? customercare@copyright.com or +1-855-239-3415 (toll free in the US) or +1-978-646-2777.

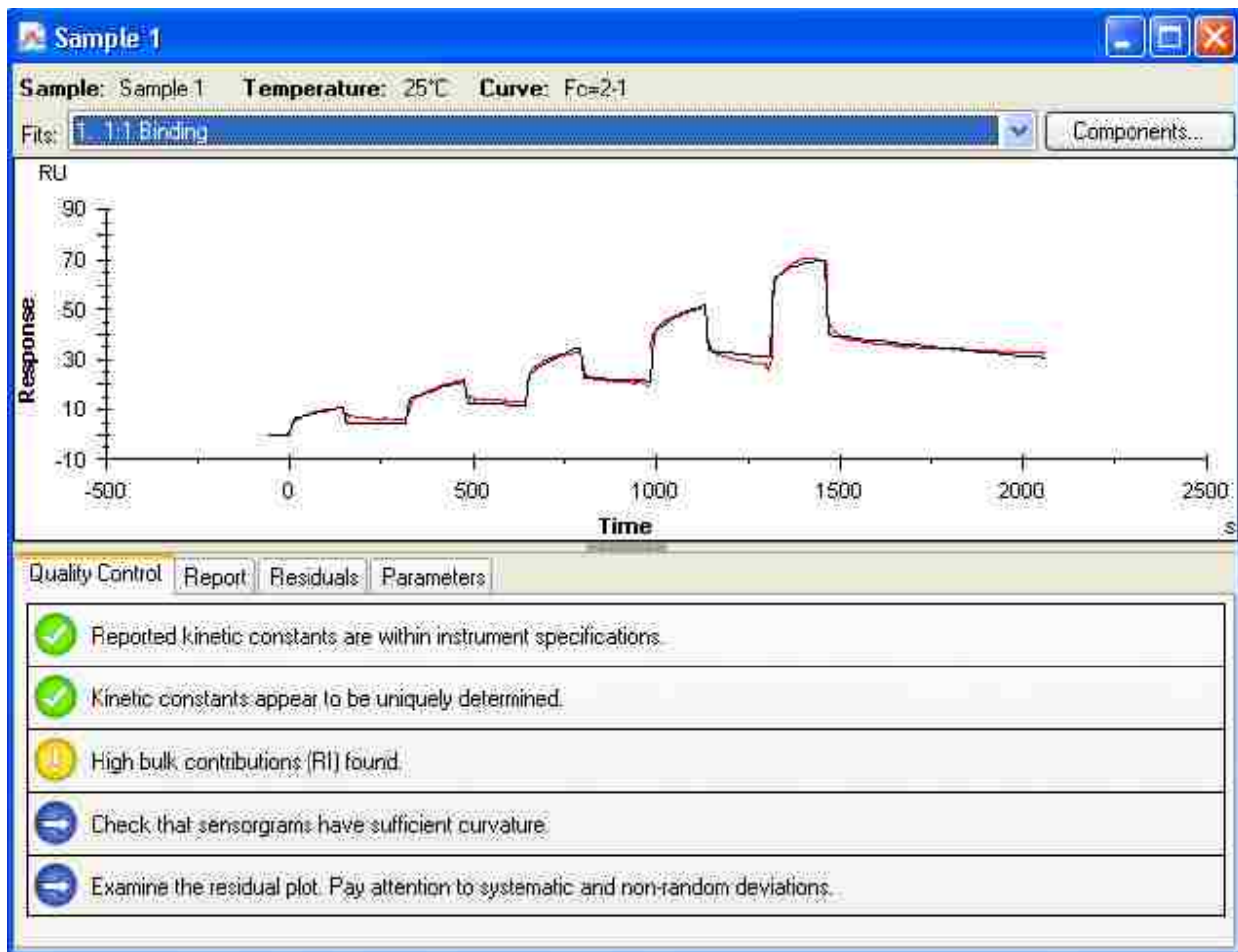## A2. Supplementary Figures: Biacore SPR Screenshots (Chapter 2)

Figure A2.1: Screenshot of the curve fit and "Quality Control" window for SPR analysis of unmodified papain with ICP K27C. Despite high bulk contributions, a unique fit was determined for the curve. The evaluation software used for this and all other SPR analyses was the on-board software provided by Biacore with instrument installation.

Figure A2.2: Screenshot of the "Report" window for SPR analysis of unmodified papain with ICP K27C. Displayed is the determined k_a and k_d values, from which the software provides a calculated K_D: 2.565×10^{-8}. Chi2 and U-values are also reported, which are measures of data quality and specificity.
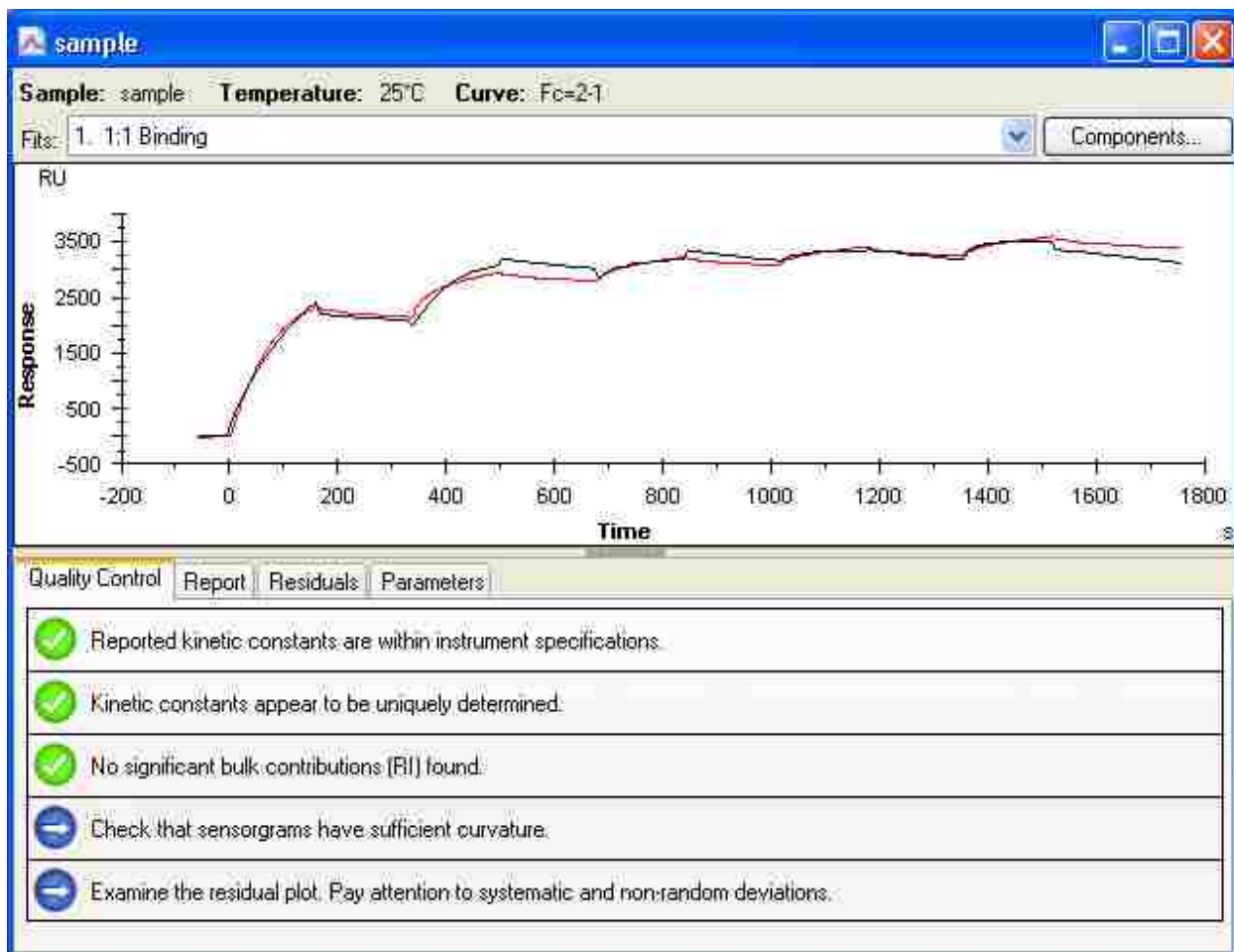
Figure A2.3: Screenshot of the curve fit and "Quality Control" window for SPR analysis of reductively methylated papain (RM-papain) with ICP K27C. No significant bulk contributions were found for this curve.

Figure A2.4: Screenshot of the "Report" window for SPR analysis of RM-papain with ICP K27C. Displayed is the determined k_a and k_d values, from which the software provides a calculated K_D: 9.43×10^{-9} M. Chi^2 and U-values are also reported, which are measures of data quality and specificity.

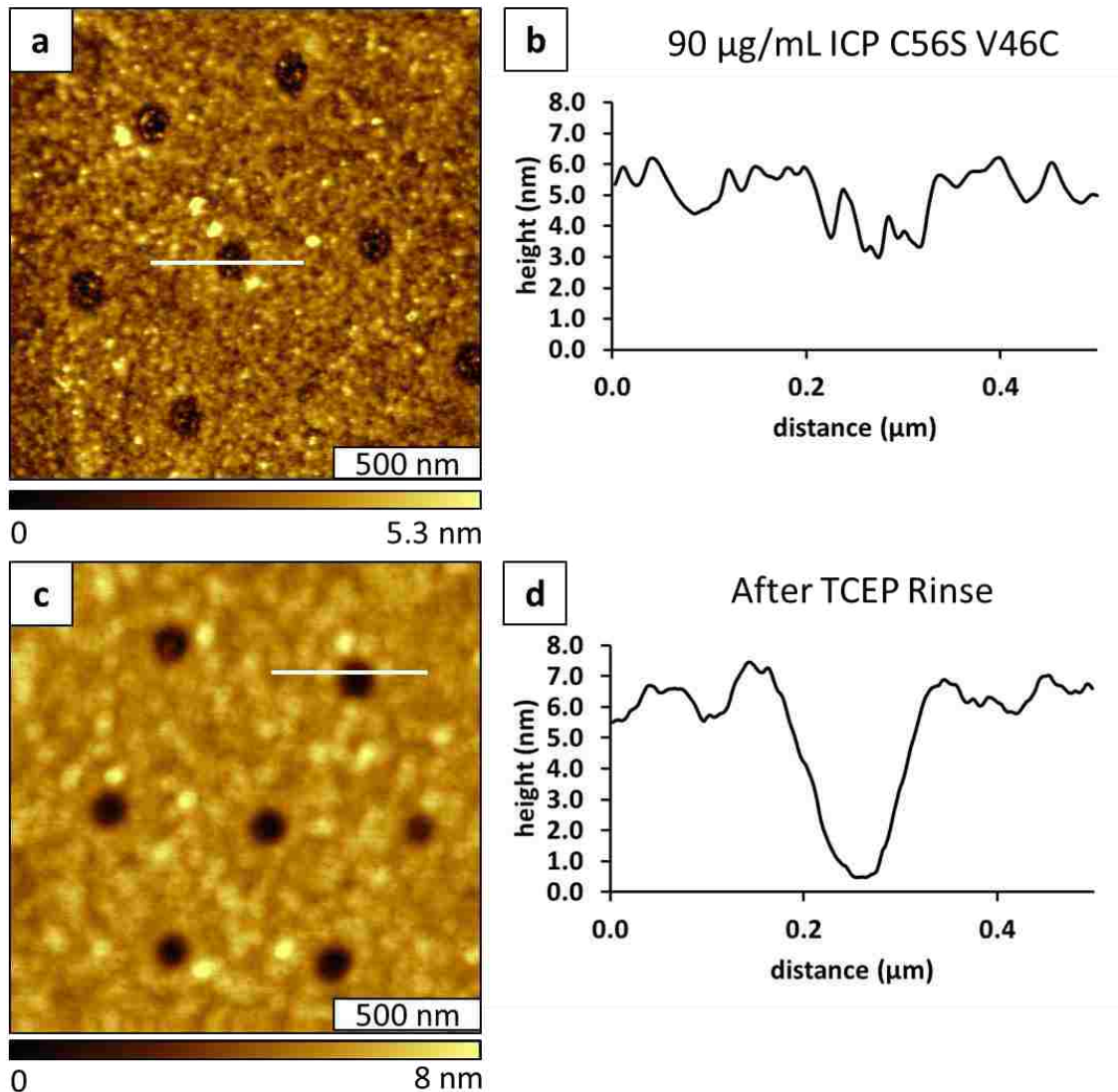**A3. Supplementary Figures: AFM Images (Chapter 4)**

Figure A3.1: Topography images of ICP anchored in MPTMS pores in PEG-silane, before (a) and after (c) substrates were rinsed with the reducing agent, TCEP. The corresponding cursor profiles (b, d) are derived from the line as seen in the topography images. These profiles show the return of nanopores on the surface when the substrate is rinsed. TCEP must reduce the disulfide bond between the cysteine residue of ICP and the free thiol within the MPTMS pores.
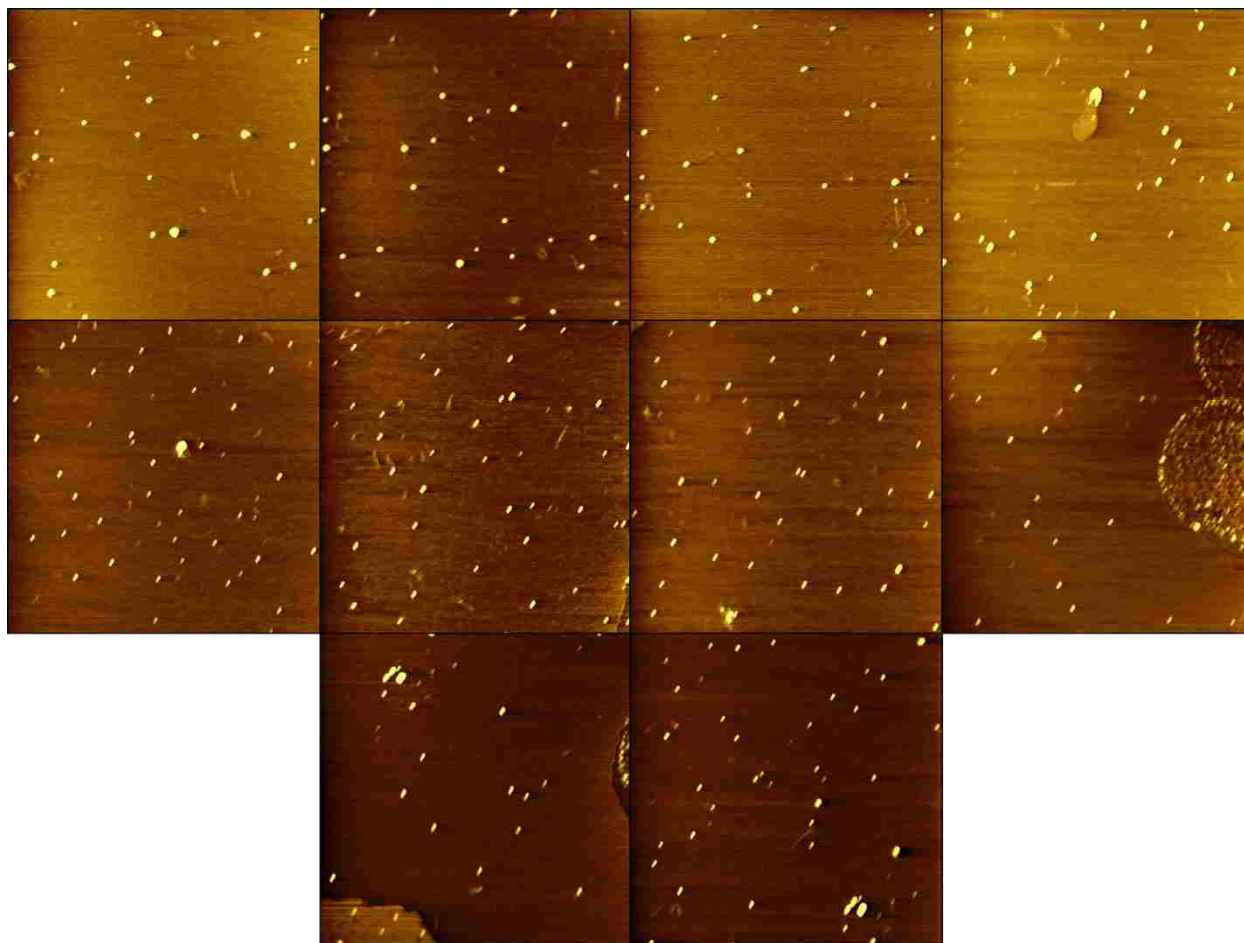
Figure A3.2: All 10 images used for the determination of average height of ICP on an ultraflat mica thin film. Each image is 3.0x3.0 µm area. Images were processed using Gwyddion software and a golden false color scale for height was applied. Lighter regions are monomers of ICP on the surface, and cursor profiles were taken for each, for a total of 100 cursor profiles.

VITA

Maggie Thomasson was born in October 1988 to Joan and Tom Thomasson. She attended high school in her hometown of Fort Mill, South Carolina. She received the state LIFE Scholarship and a Presidential Scholarship for academic excellence, and used these to attend the College of Charleston in Charleston, South Carolina in 2006. Her summers and her senior year were spent in the research lab of Dr. Wendy Cory. She graduated in 2010 with a bachelor's degree in chemistry and a minor in Spanish. She went on to pursue a doctoral degree in chemistry at Louisiana State University, where she joined the research lab of Dr. Megan Macnaughtan. She anticipates receiving her Doctor of Philosophy degree in August of 2016.